Geochemistry, Geophysics, Geosystems®

RESEARCH ARTICLE
10.1029/2023GC010884

Revealing the Extent of Submarine Permafrost and Gas Hydrates in the Canadian Arctic Beaufort Sea Using Seismic Reflection Indicators

H. Grob[1], M. Riedel[2], M. J. Duchesne[3], S. Krastel[1], J. Bustamante[4], G. Fabien-Ouellet[4], Y. K. Jin[5], and J. K. Hong[5]

[1]Kiel University, Kiel, Germany, [2]GEOMAR Helmholtz Centre for Ocean Research Kiel, Kiel, Germany, [3]Geological Survey of Canada, Quebec, QC, Canada, [4]Polytechnique Montreal, Montreal, QC, Canada, [5]Korea Polar Research Institute, Incheon, Republic of Korea

Key Points:

- Seismic reflection data reveal occurrences and extent of submarine permafrost and associated gas hydrates at the Canadian Beaufort Shelf
- Synthetic modeling of permafrost and gas hydrate is required to assess seismic processing minimizing the potential for misinterpretation
- Indicators of top and base of permafrost and the base of gas hydrate stability support previously published numerical models

Supporting Information:

Supporting Information may be found in the online version of this article.

Correspondence to:

H. Grob,
henrik.grob@ifg.uni-kiel.de

Citation:

Grob, H., Riedel, M., Duchesne, M. J., Krastel, S., Bustamante, J., Fabien-Ouellet, G., et al. (2023). Revealing the extent of submarine permafrost and gas hydrates in the Canadian Arctic Beaufort Sea using seismic reflection indicators. *Geochemistry, Geophysics, Geosystems*, *24*, e2023GC010884. https://doi.org/10.1029/2023GC010884

Received 25 JAN 2023
Accepted 22 APR 2023

Author Contributions:

Conceptualization: H. Grob, M. Riedel, S. Krastel
Data curation: M. J. Duchesne, Y. K. Jin, J. K. Hong
Formal analysis: H. Grob
Funding acquisition: M. Riedel, S. Krastel, Y. K. Jin, J. K. Hong

Abstract The Canadian Arctic Southern Beaufort Sea is characterized by prominent relict submarine permafrost and gas hydrate occurrences formed by subaerial exposure during extensive glaciations in Pliocene and Pleistocene. Submarine permafrost is still responding to the thermal change as a consequence of the marine transgression that followed the last glaciation. Submarine permafrost is still underexplored and is currently the focus of several research projects as its degradation releases greenhouse gases that contribute to climate change. In this study, seismic reflection indicators are used to investigate the presence of submarine permafrost and gas hydrates on the outer continental shelf where the base of permafrost is expected to cross-cut geological layers. To address the challenges of marine seismic data collected in shallow water environments, we utilize a representative synthetic model to assess the data processing and the detection of submarine permafrost and gas hydrate by seismic data. The synthetic model allows us to minimize the misinterpretation of acquisition and processing artifacts. In the field data, we identify features along with characteristics arising from the top and base of submarine permafrost and the base of the gas hydrate stability zone. This work shows the distribution of the present submarine permafrost along the southern Canadian Beaufort Sea region and confirms its extension to the outer continental shelf. It supports the general shape suggested by previous works and previously published numerical models.

Plain Language Summary Submarine permafrost, ground beneath the seafloor that perennially remains below 0°C, is present on the continental shelf of the Canadian Beaufort Sea. During the Late Pleistocene (~1 Million years ago), the continental shelf was subaerially exposed to the cold Arctic air causing the formation of ice in the ground. This period was followed by a sea level rise that flooded the continental shelf with warmer waters, resulting in an intensive change of the thermal regime. The relict permafrost still reacts to this thermal change and is continuously thawing. Associated with the presence of relict permafrost, extensive gas hydrates exist to >1,000 m below the seafloor. Climate warming threatens both the stability of permafrost and associated gas hydrates. Their thawing and decomposition can cause a release of greenhouse gases which in turn amplifies climate warming. This study uses marine seismic reflection data to identify permafrost and gas hydrate in the southern Canadian Beaufort Sea. We find indicators of the top and base of permafrost and the base of the gas hydrate stability zone in the outer continental shelf area. Our work shows that the permafrost and gas hydrates still extend to the outer continental shelf and thereby supports previously published numerical models.

1. Introduction

Permafrost is ground that perennially remains below 0°C (e.g., Dobinski, 2011; Osterkamp, 2001; Van Everdingen, 1998). In contrast to onshore permafrost, offshore permafrost present beneath much of the continental shelf of the Arctic is still poorly explored (Angelopoulos et al., 2020). Permafrost is increasingly becoming the focus of scientific attention because its thawing can cause emissions of greenhouse gases or result in geohazards like landslides or ground collapses (Angelopoulos et al., 2020; Natali et al., 2021; Paull et al., 2022; Schuur et al., 2015). Greenhouse gases are either trapped within the permafrost, originate from the dissociation of intra-permafrost gas hydrates, or result from microbial decomposition of newly exposed organic carbons (Ruppel & Kessler, 2017; Schuur et al., 2015). The release of carbon dioxide (CO_2) and methane (25 times more

Investigation: H. Grob, M. Riedel, Y. K. Jin, J. K. Hong
Methodology: H. Grob, J. Bustamante
Project Administration: M. Riedel, S. Krastel
Resources: M. Riedel, M. J. Duchesne
Software: J. Bustamante, G. Fabien-Ouellet
Supervision: M. Riedel, S. Krastel
Validation: M. Riedel, M. J. Duchesne, S. Krastel, G. Fabien-Ouellet
Visualization: H. Grob
Writing – original draft: H. Grob
Writing – review & editing: H. Grob, M. Riedel, M. J. Duchesne, S. Krastel, J. Bustamante, G. Fabien-Ouellet, Y. K. Jin, J. K. Hong

potent than CO_2 averaged over a century; IPCC, 2013) can increase global warming and accelerate permafrost thawing through a feedback effect. Therefore, there is a need to investigate the current submarine permafrost conditions to better constrain climate change scenarios. Gas hydrates are naturally occurring compounds in which a gas molecule combines with water in a clathrate structure under intermediate-pressure and/or low-temperature conditions (Ruppel & Kessler, 2017). Permafrost protects gas hydrates from dissociation as its cold temperatures enable a stable environment even in relatively shallow areas (Ruppel & Kessler, 2017). The stability conditions of permafrost-associated gas hydrates are threatened by increasing temperatures as a consequence of global warming and by geothermal heat and warm fluid fluxes from depth. The dissociation of gas hydrates is, at the same time, a consequence of global warming and a source through the release of greenhouse gases and large amounts of trapped carbon (Ruppel & Kessler, 2017).

1.1. Acoustic Detection of Permafrost and Gas Hydrates

The unique mechanical properties of permafrost and gas hydrates make seismic methods appropriate for remote investigations. Frozen or ice-bearing permafrost (IBPF) is any permafrost that contains ice (Harris et al., 1988). The proportion of ice, together with the sediment and pore fluid properties, determines the physical and mechanical properties of IBPF (Osterkamp, 2001). With increasing ice content, the soil particles may become ice-bonded, which means that the ice cements the sediment grains together with the pore space. Then, the physical properties like compressional and shear strengths significantly increase, whereas the porosity and permeability decrease. Therefore, "frozen" or "ice-bearing" states the existence of ice within the sediments, whereas "ice-bonding" describes the mechanical status of IBPF (Harris et al., 1988). A similar process applies to hydrate-bearing sediments, where physical properties develop analogously with increasing hydrate saturation (Yun et al., 2005).

Seismic indications for permafrost and gas hydrates are frequently reported in the literature. Evidence for IBPF in seismic data mainly stems from velocity analyses of refractions (e.g., Brothers et al., 2012; Draebing, 2016; MacAulay & Hunter, 1982; Pullan et al., 1987; Riedel et al., 2016), analysis from stacking velocities (Brothers et al., 2016), inversion applications (e.g., Kang et al., 2021; Ramachandran et al., 2011) or imaging-effects like an increased reflectivity (Hinz et al., 1998), amplitude anomalies, or travel time pull-up effects (e.g., Matson et al., 2013; Portnov et al., 2013). Reflections from the top of IBPF were noted, for example, in the Kara and Laptev Sea (Rekant & Vasiliev, 2011; Rekant et al., 2005, 2015). Reflection evidence from the base of IBPF is known from onshore seismic surveys (e.g., Dewing et al., 2016), where in contrast to offshore surveys, the absence of free-surface multiples allows to identify the base of the permafrost with relative ease (Duchesne et al., 2022).

The occurrence of marine gas hydrates is commonly inferred in seismic data by appearances of bottom-simulating reflections (BSRs) at the base of the gas hydrate stability zone (BGHSZ) (e.g., Kvenvolden, 1993; Shipley et al., 1979; Spence et al., 2010 and references therein). The presence of hydrate may also be accompanied by acoustic blanking within the hydrate stability zone (Liu et al., 2017). In a permafrost environment, a BSR is often unrecognizable, and gas hydrates are indistinguishable from ice using standard geophysical measurements (Ruppel, 2015). Besides the detection of marine gas hydrates, efforts to estimate the saturation of hydrates in sediments comprise velocity analysis of seismic reflection data (e.g., Wood et al., 1994) or seismic inversion methods (e.g., Liu et al., 2017; Westbrook et al., 2008).

1.2. Objectives

Despite industry activity and numerous vintage seismic records, few publicly available modern digital seismic records exist to evaluate offshore permafrost in the Canadian Beaufort Sea. Thus, the current state of the offshore permafrost is still not well established and remains challenging to fully appraise the role of degrading permafrost in climate change and as a potential geohazard.

In our study, we analyze seismic indicators derived from multichannel seismic (MCS) reflection data to expand the current knowledge of submarine permafrost and permafrost-associated gas hydrates on the continental shelf of the Canadian Beaufort Sea. As this is an environment where conventional seismic data suffer from free-surface and internal multiples that mask primary signals, we first assess the ability of seismic methods to detect submarine permafrost and gas hydrate by using synthetic data obtained by viscoelastic modeling. Thereby, we will review the reliability of the seismic field data after intensive data processing to minimize interpretation pitfalls.

Then, different seismic reflection indicators are investigated using our field data to infer information about the occurrence and the extent of submarine permafrost and gas hydrates at the Canadian Beaufort Shelf.

2. Permafrost and Gas Hydrates in the Canadian Beaufort Sea

The Canadian Beaufort Sea is located in the Arctic offshore the Yukon and the Northwest-Territories in Canada, close to the Canada-U.S. border (Figure 1). It extends from 141° west to Banks Island in the east and is characterized by a shallow, 100–150 km broad continental shelf before the shelf break is reached at 80–120 m of water depth (Carmack et al., 1989; Dixon & Dietrich, 1990). The Canadian Beaufort Sea shelf and slope region is one of the best-documented Arctic coastal/shelf regions due to intensive scientific research for more than 40 years and offshore exploration for hydrocarbons in the 1980s and 1990s (e.g., Dallimore et al., 2015; Dixon, 1996).

2.1. Evolution of Permafrost

Most of the present submarine permafrost is relict terrestrial permafrost (Angelopoulos et al., 2020). During the Pliocene and Pleistocene, extensive glaciations affected the Northern Hemisphere. In glacial and low sea-level periods, many marine shelves in the Arctic were subaerially exposed to current water depths of 120 m and subjected to mean annual temperatures of −20°C or colder (Brigham & Miller, 1983). These conditions favored the formation of permafrost and gas hydrates, particularly in areas that were not covered by ice for most of the Quaternary, for example, the Canadian Beaufort Shelf (Batchelor et al., 2013; Dyke, 2004). In contrast, interglacial periods and associated sea-level rise led to the inundation of the former emergent shelf areas. Increased temperatures resulted in the thawing and destabilization of offshore permafrost and gas hydrates (Lewis & Collett, 2013).

After inundation, the previous freezing air temperatures changed to present average bottom water temperatures of ∼−1°C (Brothers et al., 2016; Paull et al., 2007; Taylor et al., 1996). In the Canadian Beaufort Sea, the water column currently includes the coldest waters below the seasonal thermocline between ∼30 and 200 m with mean annual temperatures of −1.5°C and maximum temperatures at ∼350 m at 0.5°C (McLaughlin et al., 2004). The intrusion of saline oceanic water into the subsurface can thaw submarine permafrost even though negative seabed temperatures are present (Osterkamp, 2001).

The submerged offshore permafrost is still responding to the thermal change due to slow rates of heat diffusion and latent heat effects associated with thawing (Riedel et al., 2017; Taylor et al., 1996). Since the Holocene marine transgression, the present seaward extent of the >500 m thick permafrost body in the Canadian Beaufort Sea is thought to have retreated <2 km and is assumed to be located <2 km landward off the shelf edge around the 100 m isobath (Taylor et al., 2013). Collapsed seafloor depressions accompanied by volume loss, and formation and collapsing of pingo-like features (PLFs) are surficial signs of submarine permafrost degradation, which were recently observed by repeat seafloor imaging at the shelf edge (Paull et al., 2022).

2.2. Present Knowledge of Permafrost and Gas Hydrates at the Canadian Beaufort Shelf

The current extent of offshore permafrost beneath the Beaufort Shelf is extensive. Pullan et al. (1987) found by seismic refraction velocity analyses that continuous ice-bonding permafrost concentrates on the central shelf, while the ice-continuity decreases more rapidly toward the shelf edge as well as toward the Mackenzie Trough (Figure 1a). Hu et al. (2013) analyzed borehole logging data to position the base of IBPF. The data reveal a permafrost depth >500 m below the seafloor (mbsf) in the central and inner-shelf area with the deepest area beneath Richards Island (720 mbsf) (Figure 1a). The depth of the IBPF becomes gradually shallower toward the outer shelf, the Mackenzie Trough, and the Amundsen Gulf.

Based on numerical modeling, Taylor et al. (2013) and Frederick and Buffett (2015) proposed a wedge-like geometry for the relict permafrost body thinning out close to the shelf edge. The results suggest that the present seaward extent of the ice-bonded permafrost body at 134°W is at the ∼95 m isobath, and the permafrost base has raised by ∼100 m since the Last Glacial Maximum to its present depth of ∼600 m (Taylor et al., 2013).

The presence of gas hydrate in the Canadian Beaufort Sea has been inferred by MCS data and interpretations of well logs and drilling responses in offshore wells (Blasco et al., 2013; Dallimore & Collett, 1998; Majorowicz &

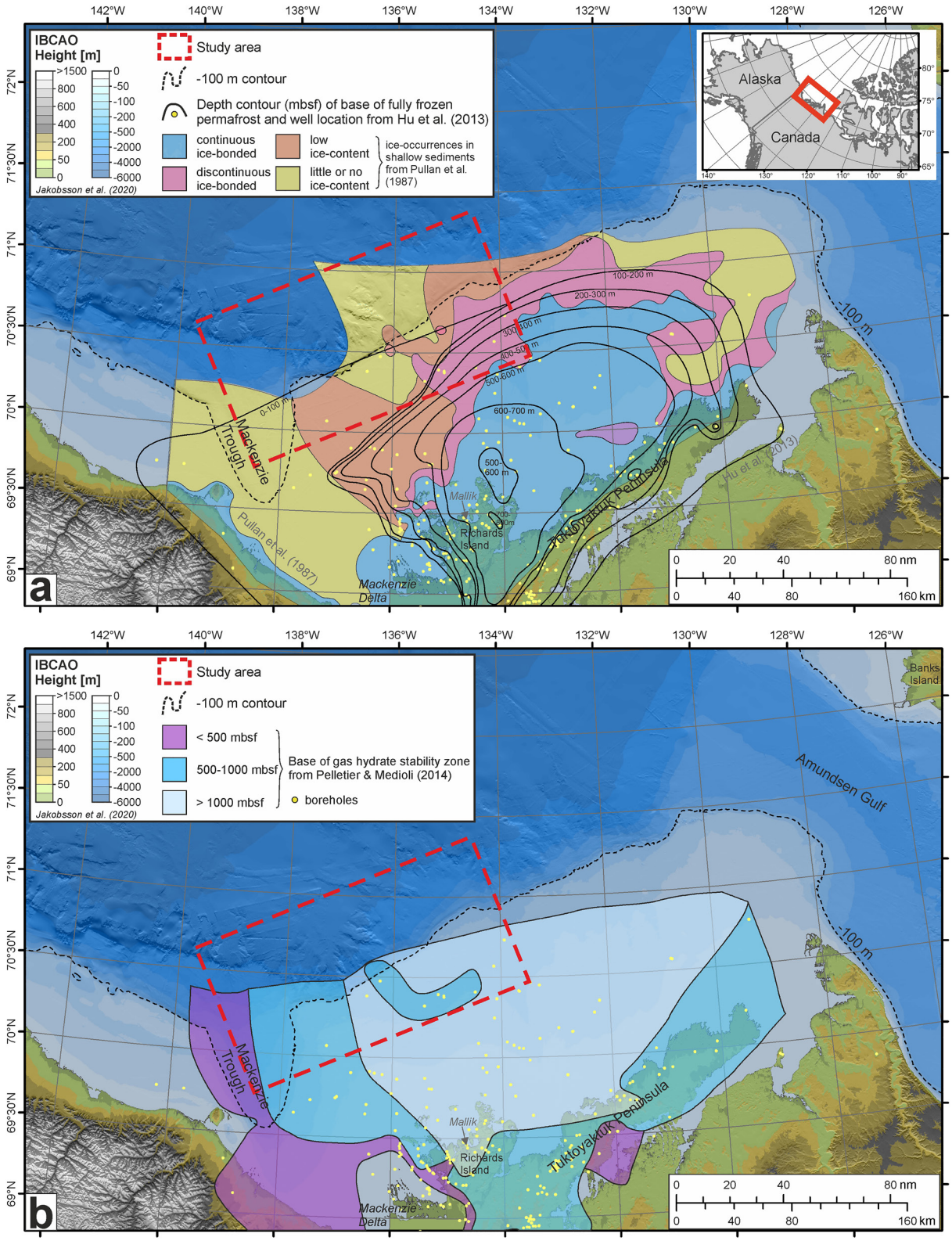

Figure 1. Overview map of the Canadian Arctic Beaufort Sea. In (a) ice-occurrences in shallow sediments determined from refraction velocities (Pullan et al., 1987) as well as the depth of the base of fully frozen permafrost determined by well log analysis (Hu et al., 2013) are shown. Panel (b) illustrates the depth of the base of the gas hydrate stability zone determined by temperature well logs (Pelletier & Medioli, 2014). A close-up of the study area is shown in Figure 2. The maps are projected in UTM8N. Bathymetry data are taken from the International Bathymetric Chart of the Arctic Ocean (Jakobsson et al., 2020).

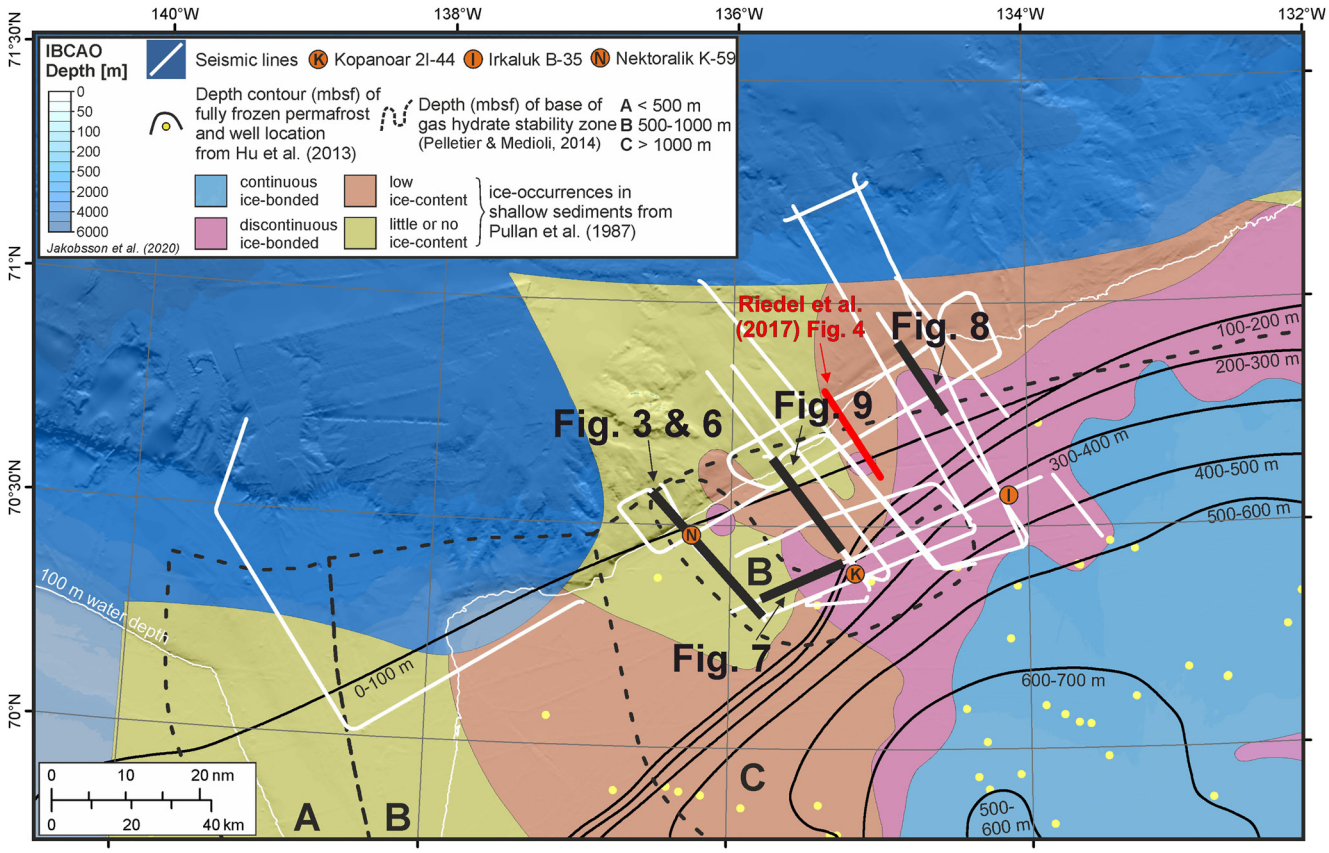

Figure 2. Close-up of the study area at the continental shelf of the Canadian Arctic Beaufort Sea. Ice occurrences and depth of fully frozen permafrost are shown as in Figure 1. The depth of the base of the gas hydrate stability zone is illustrated as black dashed lines and noted by A–C referring to different depth intervals. Seismic lines cover the outer shelf, shelf edge and continental slope.

Hannigan, 2000; Majorowicz & Osadetz, 2001; Riedel et al., 2017; Smith & Judge, 1993; Weaver & Stewart, 1982). Weaver and Stewart (1982) predicted a gas hydrate stability zone for both intra-permafrost and sub-permafrost gas hydrates between ~225 and 1,500 m depth. Riedel et al. (2017) presented the first evidence for gas hydrate occurrences within the permafrost-associated shelf and deep-water marine regions from MCS data. In contrast, gas hydrate is better constrained from seismic and well log studies onshore, for example, at the Mallik drill site (Bellefleur et al., 2007, 2012; Dallimore & Collett, 2005; Dallimore et al., 1999; Riedel et al., 2006, 2009). The current knowledge of the depth of the BGHSZ is shown in Figure 1b, based on Pelletier and Medioli (2014).

3. Data

In this study, we present sub-bottom profiler (SBP) and 2D MCS data from two research expeditions in 2013 (ARA04C) and 2014 (ARA05C) onboard the research icebreaker ARAON operated by Korean Polar Research Institute (KOPRI) (Jin & Dallimore, 2016; Jin et al., 2015) (Figure 2). Table 1 summarizes the acquisition parameters of the MCS data. The seismic survey aimed to image both the shallow subsurface and deeper geological

Table 1
Summary of Marine Seismic Acquisition Parameters of Research Expeditions ARA04C and ARA05C From Jin et al. (2015) and Jin and Dallimore (2016)

Expedition	Number of lines	Source	Shot interval (m)	Number of channels	Channel spacing (m)	Minimum offset (source—1st ch.) (m)	Record length (s)	Sample rate (ms)	Dominant frequency (Hz)
ARA04C (2013)	14	8 G-Guns: 1,200 in3 (~20 l)	93.75	120	12.5	100–110	10	1	~28
ARA05C (2014)	23	8 G-Guns: 1,200 in3 (~20 l)	50	120	12.5	85	10	1	~28

structures of the Canadian Beaufort Shelf. The vertical resolution of the MCS data is ∼13–23 m (λ/4: 28 Hz; 1,500–2,600 m/s).

The SBP data were collected during cruises ARA04C and ARA05C with a Kongsberg SBP 120 system which operates over a frequency range between 2.5 and 7 kHz that results in a vertical resolution of ∼0.5 m (Jin & Dallimore, 2016; Jin et al., 2015). The SBP data provide high-resolution information on the sediment layering within the upper ∼50–100 mbsf and complement the MCS data set.

We performed the seismic data processing with VISTA® desktop seismic data processing software. Both seismic datasets are binned to common-midpoints (CMPs) with a 12.5 m spacing resulting in average folds of 16 for 2013 and 31 for the 2014 data. The processing sequence applied to both datasets encompasses muting above the seafloor reflection, bandpass filtering, predictive deconvolution and noise muting in the slant stack domain, frequency-wavenumber (FK) filtering, surface-related multiple elimination, spherical divergence correction, interactive velocity analysis, normal-moveout correction, stretch muting and median noise attenuation (THOR; Butler, 2012) in the pre-stack domain. After normalized stacking, the data were time-migrated by a finite-difference migration algorithm and white noise was subtracted. Finally, we applied a top mute above a seafloor reflection and a time-variant bandpass filter (8/12/100/200 Hz for <∼2 s TWT).

The seismic processing improves the image quality and interpretability of the data (Figure 3). It allows to restore the shallow seafloor on the shelf and retains polarity information despite the important distance between the source and the nearest receiver. Although residual multiples persist on the seismic image of the continental shelf (see yellow boxes in Figure 3), the processing has significantly attenuated the energy of the free-surface multiples.

We used the interpretation software Kingdom™ by IHS Markit (version 2018) to interpret seismic, SBP and well log data. The bathymetry, as shown in the maps, is from Jakobsson et al. (2020).

4. Viscoelastic Modeling of Submarine Permafrost and Gas Hydrate Layers

Imaging permafrost and gas hydrates using seismic reflection data in the Canadian Beaufort Shelf is challenging because of the shallow water depth (<100 m). In shallow water, seismic surveys generate high multiple energy overprinting primary signals, particularly in the upper strata where time and moveout differences between primaries and multiples are low (Verschuur, 2013). Moreover, while on land, the ground is frozen from the surface down to the base of permafrost, a permafrost body offshore is sandwiched between unfrozen layers above and beneath. In consequence, high-energy free-surface multiples are generated not only at the seafloor but also at the top of permafrost (Duchesne et al., 2022).

Therefore, effective multiple attenuation methods are required to image reflections in the upper 1.5 s where submarine permafrost and gas hydrates are expected. However, there is a risk of damaging the seismic data using strong multiple attenuation without appropriate quality checks impeding reliable interpretation. To assess the ability of permafrost and gas hydrate detection and to review the reliability after intensive data processing, we forward model synthetic shot gathers based on the same acquisition parameters and processing steps as the field data.

4.1. Numerical Model of Permafrost and Gas Hydrates

Initially, we created a numerical model of permafrost and gas hydrates using a range of probabilistic viscoelastic properties determined from the literature (Figure 4; Bellefleur et al., 2007; Fabien-Ouellet et al., 2020; Hu et al., 2013; Johansen et al., 2003; King et al., 1988) (see Figure S1 in Supporting Information S1). We built the model according to the works of Fabien-Ouellet et al. (2020), in which the authors investigated the seismic response of a submarine permafrost environment. Table 2 summarizes the acoustic and viscoelastic properties of the media used to generate the synthetic seismic data.

The distribution of permafrost and gas hydrates was defined using available drilling data (e.g., Hu et al., 2013) and conforms to the numerical modeling by Taylor et al. (2013) and Frederick and Buffett (2015). The model geometry resembles the subsurface geometry imaged on seismic line ARA05C-6. It portrays simplified geology and wedge-like shapes of permafrost and gas hydrate bodies that thin out toward the shelf edge (Figure 4). We subdivide the permafrost into “ice-bonding” and “partially ice-bonding” (Table 2, Figure 4). According to Harris

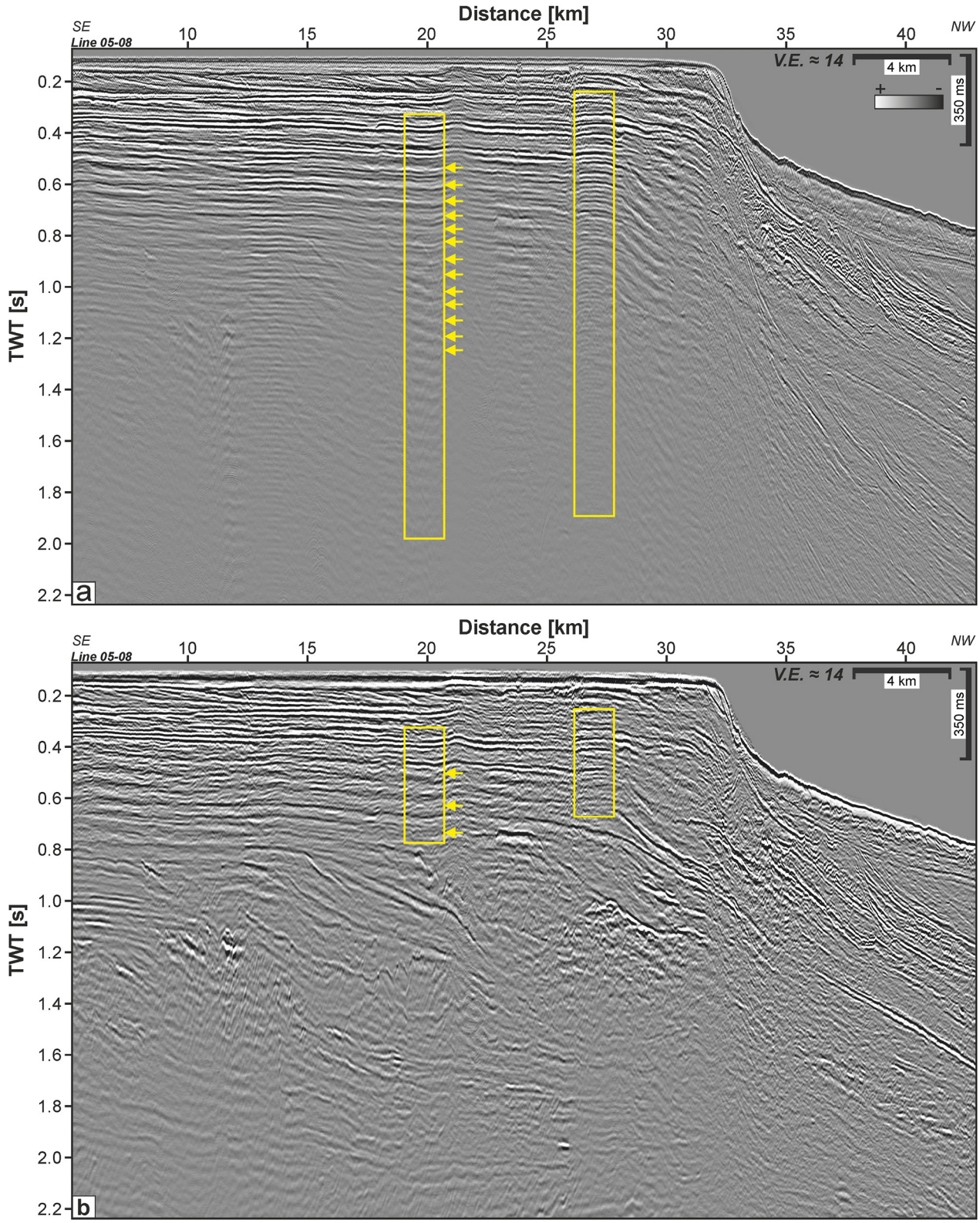

Figure 3. (a) Comparison of a conventional brute stack and (b) the corresponding final processing result of line ARA05C-08. Conventional brute stack processing: a bandpass filter, top mute, spherical divergence correction, and normal-moveout correction. A constant P-wave velocity for water of 1,500 m/s was used for the latter two. Yellow arrows point at multiples and the boxes at trains of reverberations.

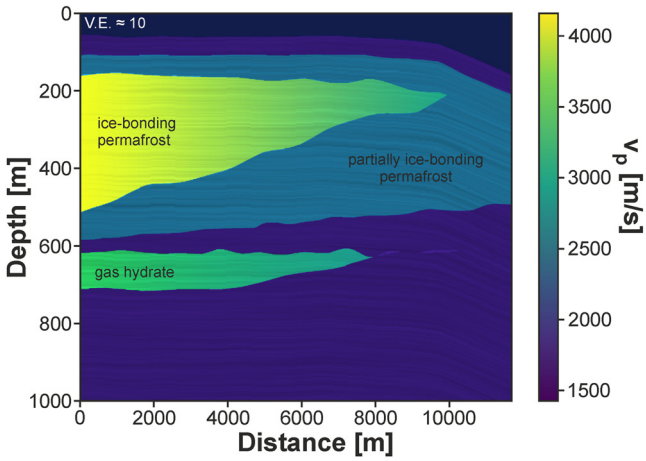

Figure 4. P-wave velocity model of partially ice-bonding and ice-bonding permafrost and gas hydrates. The gas hydrate is present as a single sub-permafrost interval.

et al. (1988), while "ice-bonding" refers to sediments strongly cemented by ice, "partially ice-bonding" refers to sediments weakly cemented by ice. A single gas hydrate interval is placed isolated beneath the permafrost body. An analog representation of isolated sub-permafrost gas hydrates can be found for example, at the Mallik Drill Site on Richards Island (see Figure 1 for location) (Dallimore & Collett, 2005). The strata represent the Upper Miocene to Pleistocene deltaic foresets of the Iperk Sequence and are modeled for the upper 1,000 m below sea level (mbsl) (Dixon et al., 1992; Paull et al., 2015) (Figure 4). The density of the background geology varies only slightly.

4.2. Synthetic Seismic Data

Based on the numerical model presented above, we generated synthetic shot gathers by solving the viscoelastic wave equation with a time-domain finite difference method after Fabien-Ouellet et al. (2017). For the modeling, source characteristics and acquisition parameters identical to the original field data were used (compare to Table 1). The CMP bin geometry was simplified to a straight line. To assess the impact of the processing, we applied the same steps to the synthetic shot gathers as used for the field data.

Based on the investigation of submarine permafrost detection through viscoelastic modeling (Duchesne et al., 2022), we expect the synthetic seismic data to have the following characteristics: (a) reflections from the top of the permafrost and gas hydrate bodies will be relatively parallel to the background geology and more challenging to identify; (b) given the wedge-like shapes of the bodies, the reflections that originate from the base of the wedges are expected to move upwards and cross-cut lithologic-related primaries and residual multiples, facilitating its detection; (c) the ice-bonding permafrost and gas hydrate wedges generally represent phase boundaries with high acoustic impedance contrasts. We expect these acoustic impedance contrasts to cause high-amplitude reflections; (d) due to velocity inversion, reflections at the base of the wedges should be polarity-reversed (relative to the seafloor reflection); (e) the reflections from the top and bottom of the partially ice-bonding permafrost are expected to have lower amplitudes and to be subparallel to the strata making the identification more challenging.

Figures 5a and 5b show the final migrated stack from the synthetic seismic data and its interpretation, respectively. The seafloor is characterized by a positive polarity reflection which is affected by shallow, vertical streaks at its onset (yellow dashed line). These vertical streaks result from a high minimum offset and a small fold, which, in turn, is related to a small bin spacing. In general, reflections dip to larger CMPs.

Two prominent reflections below the seafloor dominate the image in the upper 0.5 s. First, a high-amplitude, continuous, and positive polarity reflection runs parallel to the seafloor (Figure 5b, TPF). At CMP ~675 this reflection fades out where the second prominent reflection (BPF) terminates from beneath. The second reflection is polarity-reversed, high-amplitude and discontinuous, and cross-cuts the reflections related to the geological interfaces. Beneath, two reflections with decreased amplitude have the same dip but show alternating polarities (blue dashed lines).

Below 0.5 s, we can identify a high-amplitude, positive-polarity reflection that dips toward larger CMPs (TGH). This reflection becomes more subtle at ~CMP 550. Slightly below, a subparallel reflection has a similar appearance but with reversed polarity (BGH).

Table 2
Acoustic and Viscoelastic Properties of the Media Used for Seismic Modeling

Layer	v_P (m/s)	v_S (m/s)	ρ (kg/m^3)	Q
Water	1,430	–	1,000	1,000
Background geology	1,700 ± 200	400 ± 150	1,900 ± 150	50 ± 30
Partially ice-bonding permafrost	2,200 ± 450	790 ± 160	1,901 ± 150	20 ± 10
Ice-bonding permafrost	2,600–4,100	1,000–1,530	1,902 ± 150	25 ± 10
Gas hydrate	2,200 ± 450	790 ± 160	1,903 ± 150	20 ± 5

10.1029/2023GC010884

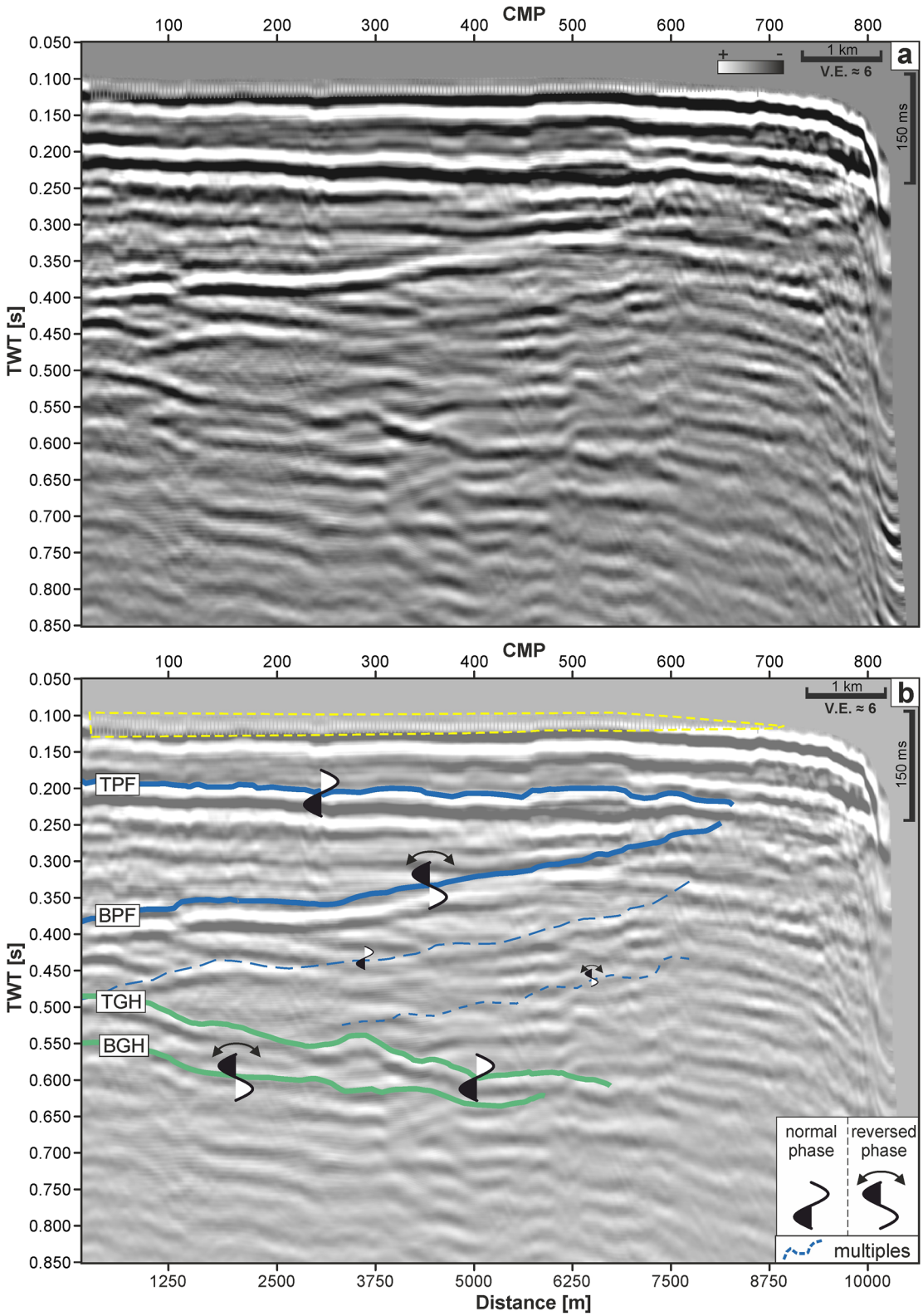

Figure 5. Final processed synthetic data (a) uninterpreted and (b) interpreted. Blue solid lines outline the top and the base of the ice-bonding permafrost body (TPF and BPF), and green lines outline the top and base of the gas hydrate interval (TGH and BGH). The dashed blue lines show multiples of the BPF. The yellow dashed line encircles the area where vertical streaks occur. Note that we inserted a white transparent background in (b) for visualization making the image appear brighter.

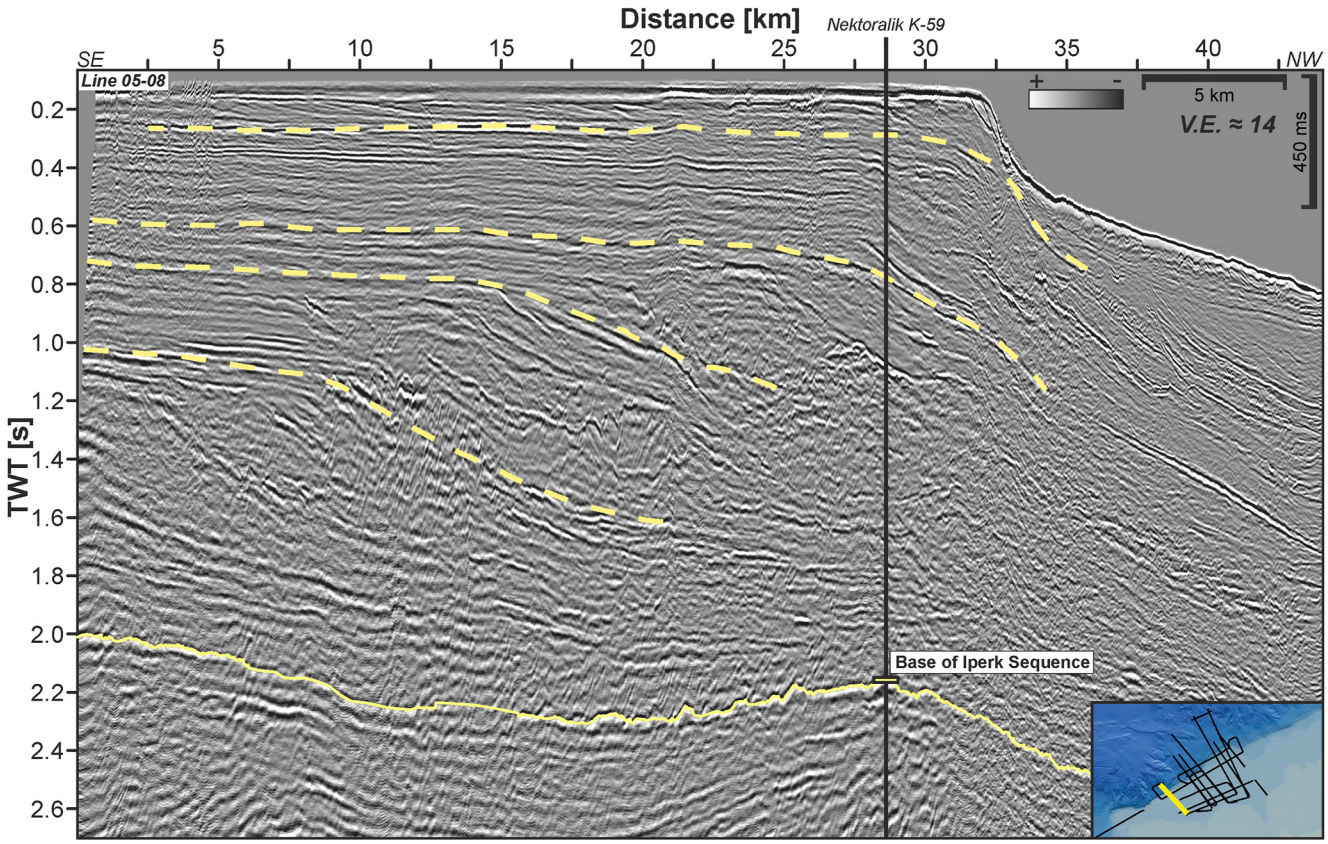

Figure 6. Seismic section from line ARA05C-08 shows the sedimentary architecture of the Iperk Sequence on the continental shelf. Yellow dashed lines indicate the deltaic prograding foresets of the sequence. Here, an automatic gain control is applied to the amplitudes to highlight the structure in the entire image. Well log information at "Nektoralik K-59" is taken from Hu et al. (2015).

4.3. Interpretation of the Synthetic Data

We identify the reflections TPF as the top and BPF as the base of the ice-bonding permafrost wedge, respectively. These reflections agree with the expected dipping and polarity characteristics described previously (Figure 5b). The reflections marked by the blue dashed lines are interpreted as multiples of the base of ice-bonding permafrost. Similarly, the reflections TGH and BGH agree with the dipping and polarity characteristics of the top and base of the gas hydrate interval. Note that no seismic reflections were found that point at partially ice-bonding permafrost.

We validated the interpretation by rebuilding the original input model based on the interpretation in Figure 5b. For this purpose, we converted the interpreted synthetic seismic image to the depth domain (see Figure S2 in Supporting Information S1). As result, the rebuilt velocity model in the depth domain (Figure S2 in Supporting Information S1) is very similar to the original input model and thus, supports the correctness of the interpretation.

5. Results

5.1. Subsurface Structure of the Canadian Beaufort Shelf

Figure 6 shows a representative seismic line running southeast to northwest across the continental shelf. This line is characterized by the broad continental shelf that turns into the continental slope toward the northwest. The shelf is underlain by the Pliocene to Pleistocene Iperk Sequence (e.g., Dietrich et al., 2011; Dixon et al., 1992; Hu et al., 2015). The nearly horizontal, parallel to subparallel reflections of the Iperk Sequence dip toward the continental slope (dashed yellow lines). The positions of the Pliocene shelf-slope margins, that is, where the horizontal reflections start to dip, shift northwards for shallower strata. This reflection pattern of deltaic prograding foresets (compare to Patruno et al., 2015) is characteristic of the overall stratigraphic structure and the geometry

of the Canadian Beaufort Shelf (Dixon et al., 1992). Major tectonic deformation is missing in the Iperk Sequence (e.g., Dixon et al., 2019; Lane & Dietrich, 1995) (Figure 6). The depth of the base of the Iperk Sequence at ~2 s (Figure 6) increases toward the continental slope (e.g., Dietrich et al., 2011; Hu et al., 2018).

5.2. Seismic Reflection Character of the Canadian Beaufort Shelf and Slope

Figures 7–9 show three examples of seismic sections along and across the Canadian Beaufort Shelf. First, we show one section that is parallel to the shelf edge (Figure 7), and second, we show two sections across the shelf margin running to the continental slope (Figures 8 and 9). Note that we only investigate strata of the Iperk sequence in all seismic sections. Figures 7a and 9a show the co-located SBP data.

5.2.1. Seismic Line Along the Continental Shelf

The seismic line in Figure 7 runs parallel to the continental shelf edge. It is situated further landward on the shelf. The seafloor is generally flat, except for a minor depression at 23 km (Figure 7a). Reflections from the Iperk Sequence are mostly horizontal, parallel and well-stratified.

In Figures 7c and 7d, we can observe a reflection at ~1 s along the line that separates an undulating parallel reflection package above from a more chaotic package below (green dashed line). The reflection runs rather layer-parallel and shows negative-polarity bright spots beneath (arrows). The reflection is not visible between 20 and 22.5 km. Blue zones in Figure 7d indicate low amplitude areas, and yellow dashed lines show where horizontal reflections are pulled upwards. Outside the blue zones, these reflections are pushed downwards, and the amplitude level increases.

Figures 7a and 7b show the SBP and seismic data using a lower gain display. A shallow, polarity-reversed reflection at 0.1–0.15s shows a high amplitude (orange dashed line) above the low amplitude area at 15.5–23 km. There, the maximum depth of the acoustic penetration in the SBP section mirrors this high-amplitude reflection (red dotted line and *-inset in Figure 7a).

5.2.2. Seismic Lines Across the Continental Shelf

The seismic section in Figure 8 is located in the northeast part of the study area. The seismic line runs from the flat continental shelf in the southeast across the shelf edge to the continental slope in the northwest. Prograding foresets of the Iperk Sequence dipping toward the slope are characteristic of the subsurface (yellow dotted lines, Figure 8b). We can observe two faintly recognizable reflections (light blue and light green dashed lines) becoming gradually shallower toward the slope and cutting the reflection pattern attributed to the sedimentary architecture similar to the BPF reflection in Figure 5b and the BGHSZ interpreted by Riedel et al. (2017).

The deeper faint reflection (light green, Figure 8b) is most likely to be recognized between 0.92 and 0.87 s at 50–52.5 km, where it shows a slightly increased amplitude and negative-polarity. The reflection can be traced from ~1.2 s at 37.5 km to the north upwards to about 0.55 s at 55 km, where an area of decreased amplitude and reflectivity occurs. Above this area, seabed features are encountered which were interpreted as PLFs by previous works (Gwiazda et al., 2018; Paull et al., 2022). The shallower faint reflection (light blue dashed line) shows similar reflection characteristics as the deeper reflection and is most likely to be recognized between 0.48 and 0.3 s from 36 to 45 km. The reflection also becomes gradually shallower toward the northwest and cross-cuts reflections of the Iperk Sequence. By applying a frequency-wavenumber filter on the post-stack section depressing 70% of the positive dips, the reflection becomes more visible and seems to have negative polarity (inset in Figure 8b). In addition, industrial 3D seismic data presented in Riedel et al. (2017) show a similar cross-cutting reflection in the same depth range (Figure 8a* and Figure S3 in Supporting Information S1). There, the reflection also moves gradually upwards toward the northwest (light-blue arrows).

Another shelf-crossing seismic section is shown in Figure 9. PLFs imprint the flat seafloor morphology at the shelf edge (Figures 9a and 9c). Again, prograding foreset reflections characterize the Iperk Sequence (yellow dotted lines). Here, we observe only one reflection that becomes gradually shallower toward the slope and cross prograding foreset reflections (light green dashed line in Figure 9c). We infer similar reflection characteristics like cross-cutting and negative polarity in this image that was described previously for Figure 8.

As mentioned, we do not observe a shallow reflection similar to the blue dashed reflection in Figure 8b. However, a deeper cross-cutting reflection (green dashed line) similar to the BGHSZ interpreted by Riedel et al. (2017) runs

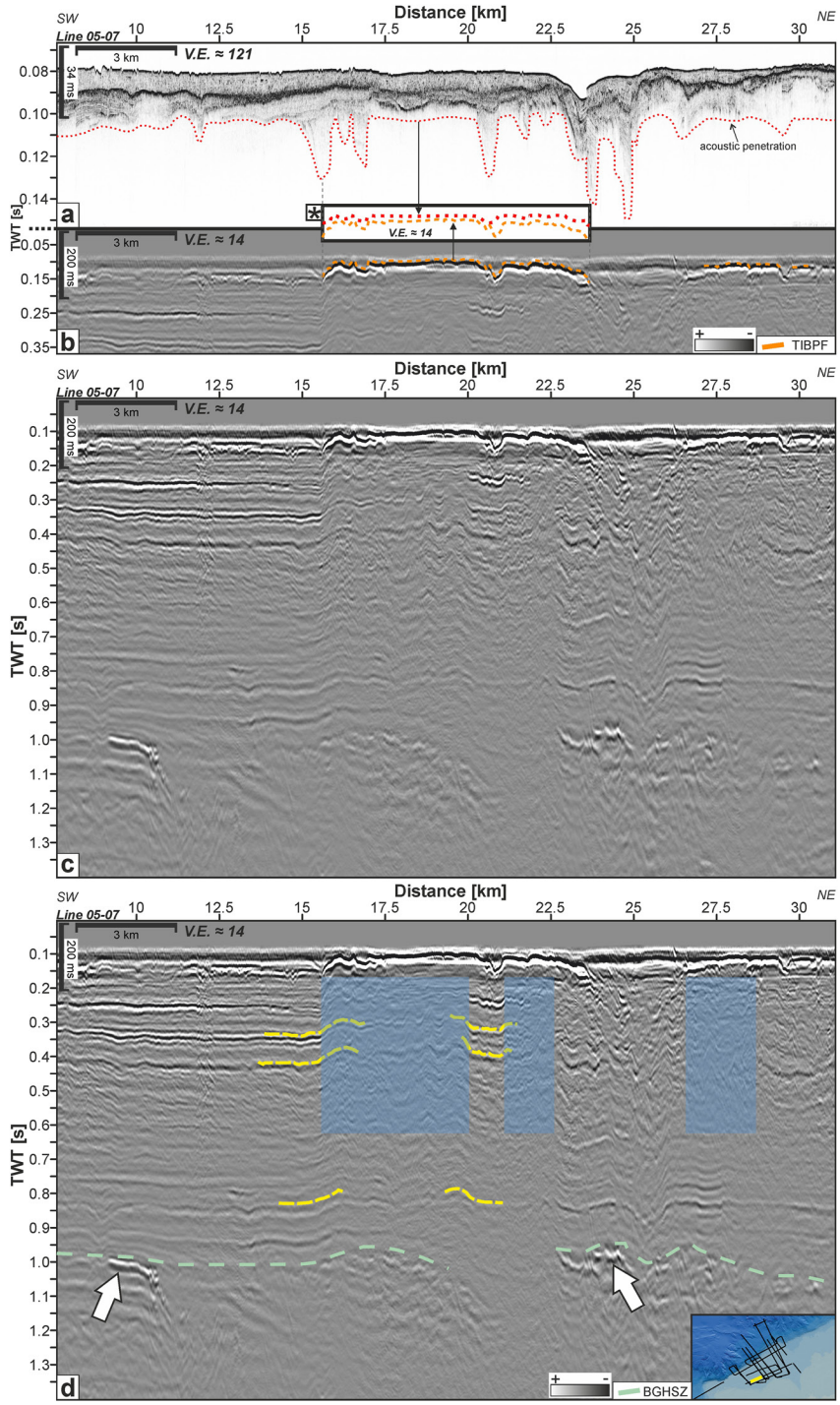

Figure 7. Co-located sub-bottom profiler (a) and seismic section ARA05C-07 (b–d) without interpretation in (c), with interpretation in (d). In (b), the upper ~0.35 s TWT of (c) are shown with reduced gaining display. The orange dashed lines indicate high-amplitude near-seafloor reflections (TIBPF), while the red dotted line in (a) delineates the maximum depth of acoustic penetration. In the inset (*), these lines are shown with equal vertical exaggeration. In (d), the yellow dashed lines highlight the prevailing stratigraphy. The dashed light-green line indicates the base of the gas hydrate stability zone. White arrows point at bright spots of negative polarity. Blue zones illustrate areas of decreased amplitudes.

10.1029/2023GC010884

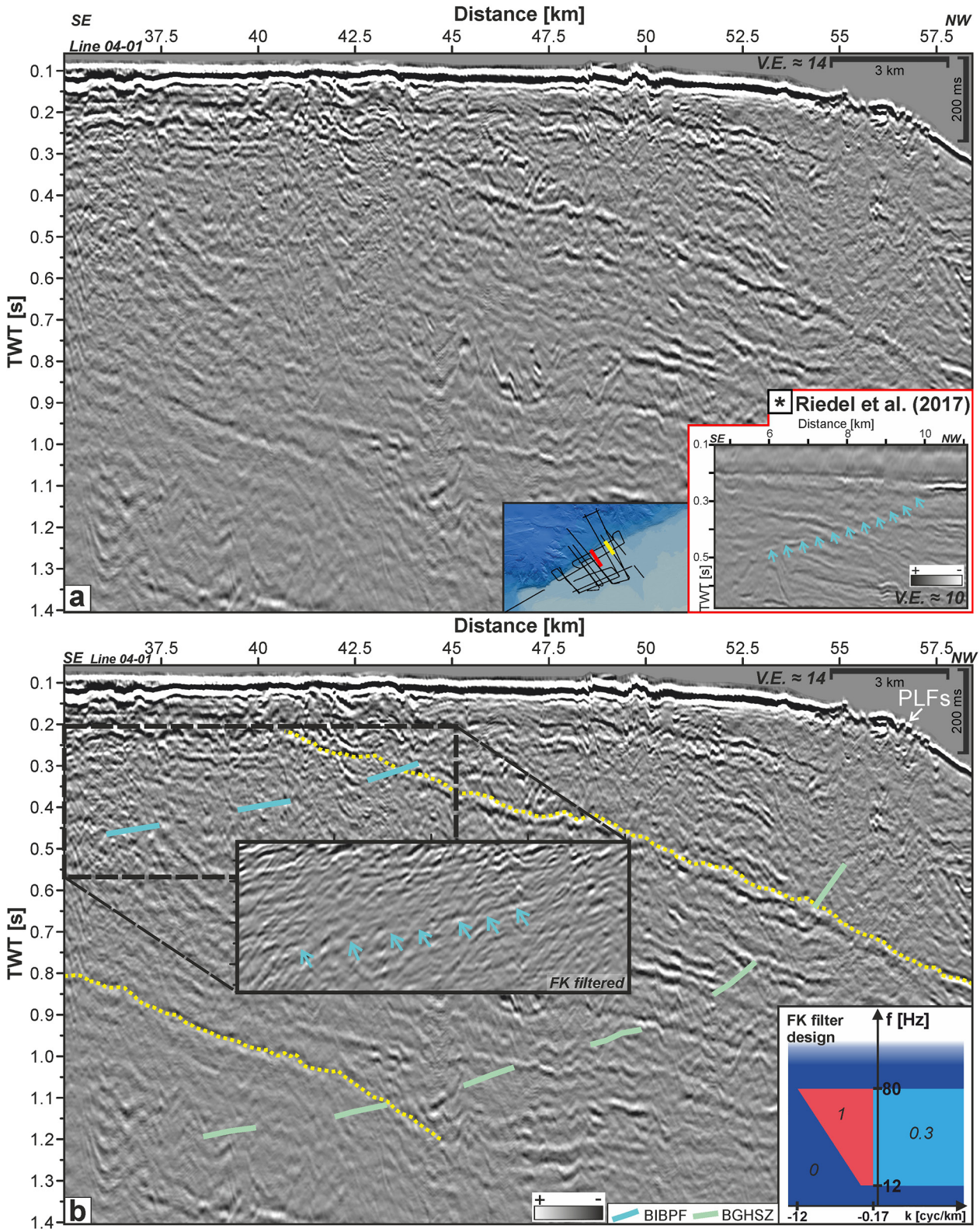

Figure 8. Seismic section from line ARA04C-01 across the Beaufort Shelf from SE to NW without interpretation in (a) and with interpretation in (b). In (a*), an adapted extract of Figure 4 from Riedel et al. (2017) is shown with permission from Elsevier and its location is marked as a red line in the mini-map. In (b), yellow dotted lines show the sedimentary architecture. The dashed lines frame indications for the base of ice-bearing permafrost (BIBPF, light blue) and the base of the gas hydrate stability zone (light green). The inset in (b) has undergone further filtering in the frequency-wavenumber (FK) domain according to the shown FK filter design. In the FK spectrum, values represent the filter-passing factors, that is, 0 is fully muted and 1 is fully preserved. PLFs, pingo-like features.

10.1029/2023GC010884

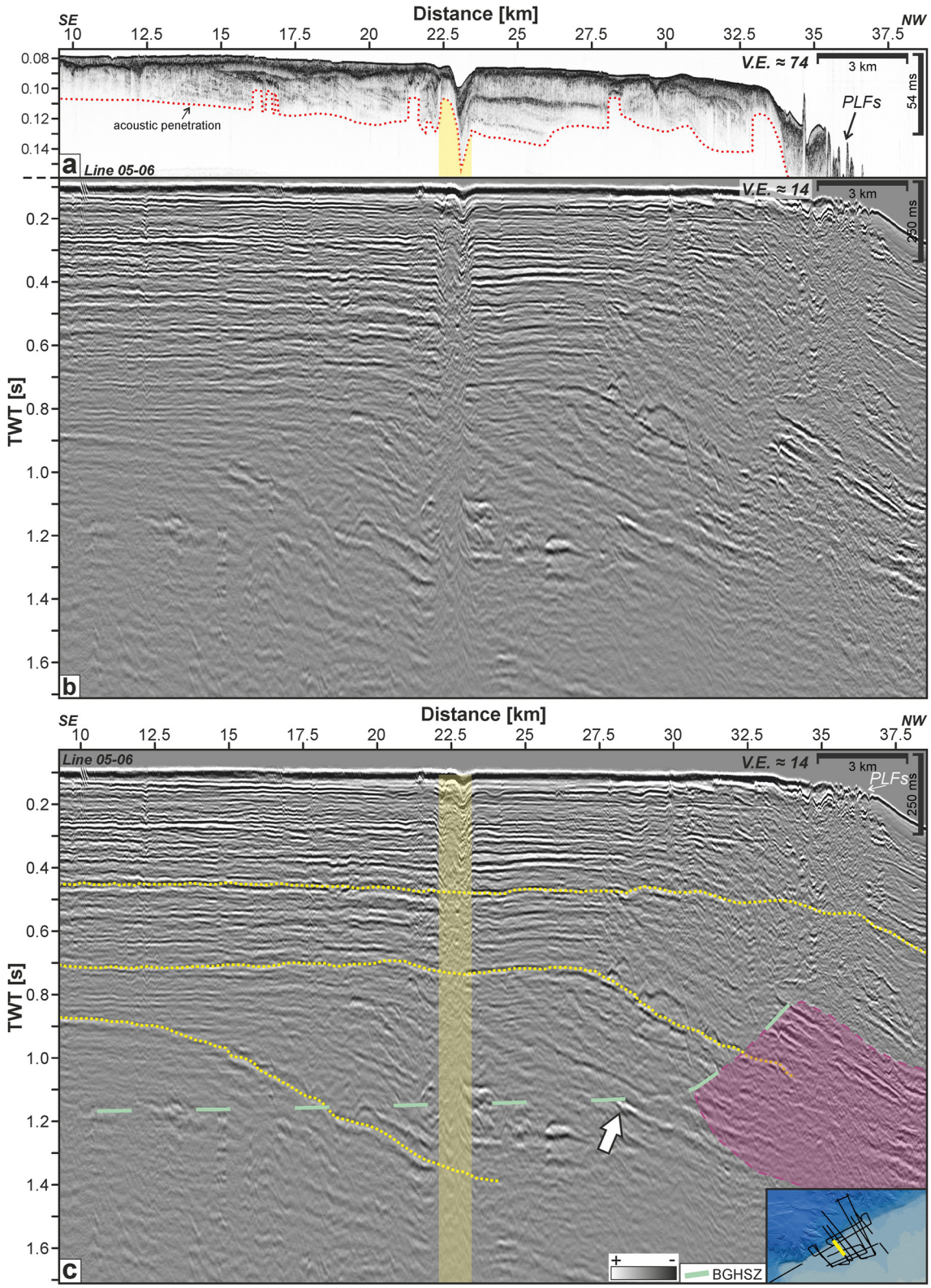

Figure 9. Co-located sub-bottom profiler data (a) and seismic section ARA05C-06 without interpretation (b) and with interpretation (c). In (a), the red dotted line shows the maximum acoustic penetration, and a yellow zone displays the same position as the yellow zone in (c). In (c), the yellow zone illustrates disturbed reflections, and the purple zone illustrates enhanced amplitudes. The yellow dotted lines show the sedimentary architecture. The light green-colored dashed line indicates the base of the gas hydrate stability zone (light green). The white arrow points at a typical bright spot. PLFs, pingo-like features.

horizontally at ~1.17 s between 10 and 31 km, where it then becomes gradually shallower to ~0.8 s at approximately 34.5 km. Below the PLFs, the seismic image has a reduced reflectivity and the cross-cutting reflection is lost. Furthermore, we can observe a negative-polarity bright spot (white arrow) and a zone of enhanced amplitudes (purple shaded area, Figure 9c) beneath the cross-cutting reflection. A vertical zone of disturbed reflections can be observed in the middle of the shelf (yellow area). These disturbed reflections (Figure 9c) coincide with a depression visible in the SBP data at 23 km (Figure 9a). At the depression at 23 km, the maximum depth of acoustic penetration (red dotted line) varies within 1 km distance from locally reduced to significantly increased (yellow zone in Figure 9a).

6. Interpretation of Seismic Indicators

6.1. Top of the Ice-Bearing Permafrost

The presence of IBPF in the subsurface is suggested by different seismic characteristics. The maximum depth of acoustic penetration in Figure 7a shows a very similar shape to a shallow high-amplitude reflection (see *-inset in Figure 7a). It suggests that the same physical cause controls the reflection event and acoustic penetration of the SBP. Moreover, the vertical zone of disturbed reflections in Figure 9c (yellow zone) suggests a high lateral velocity contrast close to the seafloor. At this location, the depth of the acoustic penetration of the SBP data varies significantly beneath the seafloor depression (red dotted line at the yellow zone, Figure 9a). Both the variation in acoustic penetration and the disturbed reflections are indicative of a juxtaposition of higher and lower seismic velocities, which likely represent frozen and less frozen or unfrozen ground. Note that Riedel et al. (2014) also inferred a relationship between the maximum depth of acoustic penetration in SBP data and the occurrence of ice. As both the high-amplitude reflection and the coinciding character of the acoustic penetration are the shallowest indications for the presence of IBPF, we interpret the high-amplitude reflection (TIBPF, Figure 7b) to represent the top of IBPF.

6.2. Base of the Ice-Bearing Permafrost

The presence of IBPF is further indicated by laterally confined high-velocity zones. Highly reflective pull-ups (yellow dashed lines, Figure 7) followed by reduced amplitudes (blue zones, Figure 7) are indicative of locally high velocities. In Figures 8 and 8a*, shallow cross-cutting reflections (light-blue dashed line/light-blue arrows) indicate phase boundaries that are not related to the Iperk Sequence. The shallow cross-cutting reflections are analogous to what is observed in the synthetic seismic data (Figure 5b) and are interpreted as the base of the IBPF. Their reversed polarity is indicative of a phase boundary corresponding to a velocity inversion indicative of a decrease in ice saturation. The base of the IBPF is around max. 0.5 s TWT.

6.3. Base of the Gas Hydrate Stability Zone

Similar to the base of IBPF, the deeper cross-cutting reflections illustrated by light-green dashed lines (Figures 8 and 9) are also indicative of a phase boundary that cross-cut reflections attributed to the Iperk Sequence. In correspondence with the interpretation of Riedel et al. (2017), the interpretation in Figure 5b and the reflections' depths, we interpret these reflections as the BGHSZ. Beneath the BGHSZ, higher amplitudes (purple area, Figure 9) and chaotic reflectivity (Figure 7) suggest changing acoustic properties. There, reversed polarity bright spots and enhanced amplitudes may indicate free gas trapped at the BGHSZ (Figures 7 and 9). The maximum depth of the BGHSZ in Figures 8 and 9 is ~1.2 s TWT and in Figure 7 ~1 s TWT. Moreover, the ascendance of the BGHSZ in Figures 8 and 9 toward the continental slope is characterized by a weak reflectivity where PLFs overlie. The weak reflectivity, together with the PLFs at the seafloor, can indicate mobilized fluids, which were released by decomposing permafrost and gas hydrates (see Gwiazda et al., 2018; Paull et al., 2007, 2011, 2022).

7. Discussion

7.1. Seismic Imaging of Submarine Permafrost and Associated Gas Hydrates

The synthetic data (Figure 5) show the capability of seismic data to detect submarine permafrost and gas hydrate reflections in a context similar to the Canadian Beaufort Sea. Even after intensive seismic processing, we are able to detect permafrost- and gas hydrate-related reflections in an ideal and simplified shallow subsurface. This

exercise also allows for minimizing interpretation pitfalls in the field data arising from acquisition and processing artifacts.

Even though adjusting acquisition parameters could improve permafrost imaging, for example, by reducing the minimum offset (Duchesne et al., 2022), residuals of free-surface and internal multiples remain the main obstacle to interpretation. Because near-horizontal and well-stratified strata complicate the identification of a near-horizontal permafrost reflection (see Figure 7 and Duchesne et al., 2022), the gradually upwards bending, cross-cutting reflection characteristics of the interpreted permafrost and gas hydrate reflections toward the shelf edge (Figures 8 and 9) allow the differentiation of these phase-boundaries from lithology-related primary and multiple reflections. In addition, a BSR at the inner Beaufort Shelf in near horizontal and well-stratified strata can be traced with confidence for the BGHSZ at the shelf edge (Riedel et al., 2017). Therefore, we argue that the reflections in the field data presented in the sections above are related to permafrost and gas hydrate occurrences. Each of those reflections is observable in different seismic datasets (ARA04C, ARA05C, and industrial 3D seismic data shown in Riedel et al., 2017). In the following, we discuss the seismic indicators of permafrost and gas hydrates.

7.2. Seismic Indicators for Permafrost and Gas Hydrates

7.2.1. The Top of Ice-Bearing Permafrost

Similar to Figure 7b, we interpreted shallow high-amplitude reflections as the top of IBPF along all other MCS lines (compare Figures S6–S22 in Supporting Information S1). Their locations along those lines are shown as red lines in Figure 10a and their depths in Figure 10b. The depth of the top of IBPF ranges between 0.106 and 0.175 s TWT (corresponding ∼100–200 mbsl at well Kopanoar 2I-44) varying locally without any recognizable trend. The locations tie well with the published map showing the ice occurrences in Pullan et al. (1987). Where Pullan et al. (1987) delineate low or no ice content, we do not find many reflections of the top of IBPF (orange and yellow zones in Figures 10a and 10b). In the eastern study area, the top of IBPF reflections occurs more frequently where Pullan et al. (1987) interpreted the presence of discontinuous ice-bonded sediments (blue and purple zones). Near the bathymetric 100 m contour to the west, sporadic top of IBPF reflections may also point at frozen sediments, for example, at PLFs (compare Figure 8 and Figure 9). However, these frozen sediments are not necessarily relict permafrost and are likely recently frozen. Paull et al. (2022) associated the origin of PLFs at the shelf edge with groundwater ascending and freezing at the seafloor when in contact with the ∼−1°C cold seawater. The ascending groundwater may originate from thawed permafrost (Paull et al., 2022).

The top of IBPF normally shows a high amplitude with positive polarity as expected from the positive impedance contrast to high velocities (TPF in Figure 5b and Duchesne et al., 2022). However, in some of our examples, the top of the IBPF reflection can exhibit a negative polarity above a high-velocity zone, which appears counterintuitive (orange dashed line, Figure 7b). Different reasons may be responsible for the polarity reversal. First, the large distance to minimum offset in combination with shallow reflectors will quickly cause overcritical reflections, which may present negative reflection coefficients as they become complex (e.g., Zhang et al., 2018). Second, a tuning effect can be observed for different frequency bands (e.g., Dondurur, 2018; Sheriff & Geldart, 1995). For instance, while the seismic image with the entire signal frequency band shows a negative polarity of the top of IBPF, a bandpass-filtered image with corner frequencies of 30/45/80/100 Hz shows a positive polarity (see Figure S4 in Supporting Information S1). And third, information from borehole Irkaluk B-35 (Hu et al., 2015) indicates a low-velocity interval below a high-velocity interval close to the top of an IBPF reflection further to the east (Figure 2; see Figure S5 in Supporting Information S1). This would cause a negative impedance contrast.

7.2.2. The Base of Ice-Bearing Permafrost

In the synthetic seismic data (Figure 5), we only observe a base of permafrost reflection at the transition from ice-bonding to partially ice-bonding. This reflection has a high amplitude and a negative polarity. In contrast, the reflections interpreted as the base of ice-bearing permafrost (BIBPF) in Figures 8a and 8a* are faint and additionally, not observable in every seismic line (compare Figure 9). Two simplifications in the input model in Figure 4 can explain this discrepancy: a homogenous lithology and sharp variations of ice-/hydrate saturation. First, whereas the input model reflects a homogeneous lithology, the Iperk strata on the mid and outer Canadian Beaufort Shelf are heterogeneous and consist of shale and sandstone intervals separated by a clay- and silt-dominant interval (Dixon et al., 1992). Duchesne et al. (2022) showed that lithology severely impacts the seismic response

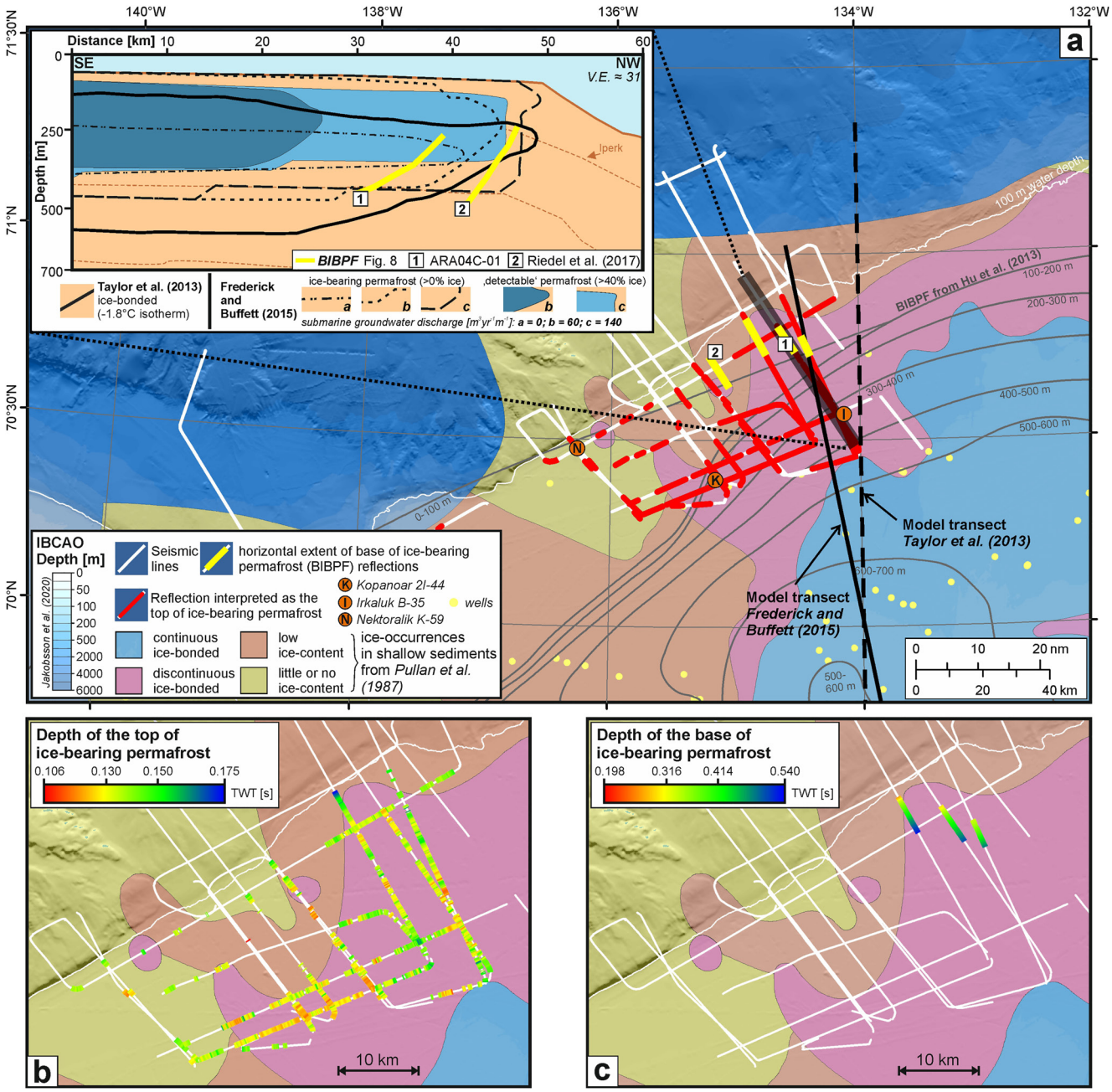

Figure 10. Location and depth of seismic indicators of submarine permafrost found in this study. In (a), red lines on the map show the interpreted top of ice-bearing permafrost (TIBPF) reflections. In the sketch, the base of ice-bearing permafrost (BIBPF) reflections (yellow solid lines) are compared to results from numerical modeling from Frederick and Buffett (2015) and Taylor et al. (2013). The corresponding positions of the BIBPF reflections are projected into the sketch, assuming that 1s TWT corresponds to 1,000 m depth (Irkaluk B-35 in Hu et al. (2015)). The structure and position of the sketch are based on Figure 8. The different extents of permafrost shown in the sketch from Frederick and Buffett (2015) depend on the volume of submarine groundwater discharge (see legend). The locations of the base and top of the IBPF reflections are shown on the map as yellow and red lines. In (b) and (c), the depths of the TIBPF and of the BIBPF reflections, respectively, are shown in TWT.

of frozen layers. They found that the energy of free-surface and internal multiples masking primary signals varies essentially depending on the type of frozen lithology. Second, unlike in the input model, where abrupt changes in seismic velocities are caused by abrupt changes in ice-/hydrate saturation, the transition from ice-bonded to partially ice-bonded (slushy) permafrost likely occurs gradually as noted by Taylor et al. (2013) and observed by Hu et al. (2013). Those slushy boundaries would show small reflection coefficients and could explain the absence of a distinct base of IBPF reflection in some seismic lines. Hence, permafrost reflections are likely less distinct

than the results from the synthetic seismic data in Figure 5 suggest. Nevertheless, we found two more reflections in the seismic data similar to Figure 8 that we interpret as the base of IBPF (Figures 10a and 10c; Figures S23 and S24 in Supporting Information S1).

In Figure 10c, the depths of the three BIBPF reflections are shown in TWT. All three reflections show comparable depths but are found at different distances to the shelf edge. However, the upwards movements of the reflections seem to follow a similar gradient.

7.2.3. The Extent of Permafrost

The sketch in Figure 10a summarizes the BIBPF reflections of Figure 8 and the permafrost limits from published numerical modeling (Frederick & Buffett, 2015; Taylor et al., 2013). The latter comprises the ice-bonding permafrost limit as −1.8°C isotherm (Taylor et al., 2013) and different permafrost limits from Frederick and Buffett (2015). The latter permafrost extents reflect two different ice saturations (IBPF of >0% and detectable permafrost >40% ice content) for different submarine groundwater discharges (a–c: 0–140 $m^3\ yr^{-1}\ m^{-1}$). The BIBPF reflections depicted in Figure 8 are projected into the sketch (Figure 10a, yellow solid lines), concerning the shelf edge position and assuming that 1 s TWT corresponds to 1 km depth (Irkaluk B-35, Hu et al., 2015).

The upward movement of the BIBPF-interpreted reflections near the shelf edge (Figures 10a and 10c) is in accordance with the numeric modeling results from Taylor et al. (2013) and Frederick and Buffett (2015). While they all differ in the order of ∼150 m vertical and ∼10 km lateral, an in-depth comparison of the different limits is not reasonable. First, because the locations of the model transects and seismic lines differ in azimuth and position, and second, it is not clear what permafrost limit is represented by the BIBPF reflection, as will be discussed in the following section.

Therefore, we argue that the indications for permafrost found in our study support the modeling results of Taylor et al. (2013) and Frederick and Buffett (2015). The upward bend of the permafrost base toward the continental slope and the approximate permafrost limit within ∼10 km of the shelf edge is consistent with the numerical modeling results and our observations (Figures 10a and 10c).

7.2.4. Ambiguous Base of Permafrost

Hu et al. (2013) analyzed geophysical well logs and temperature surveys and investigated the depth of IBPF for the Beaufort-Mackenzie Basin. The authors further distinguished between fully frozen IBPF ($IBPF_F$), which they identified by sharp changes in acoustic and electrical properties, and partially frozen IBPF ($IBPF_P$) underneath, which causes a more gradual decline in these properties. Hu et al. (2013) suggested that the base of $IBPF_F$ could represent the base of ice-bonded permafrost but emphasized missing evidence. The depths of $IBPF_F$ and $IBPF_P$ are at well Kopanoar 2I-44 (Figure 2) 305 and 395 mbsl, respectively, and at well Irkaluk B-35 (Figure 2) 392 and 468 mbsl (Table 3 in Hu et al. (2013)). If we estimate the depths of the identified BIBPF reflections (Figures 8 and 8a*) based on the time-depth chart of the Irkaluk/Kopanoar wells, their inferred maximum depths are ∼480 mbsl (∼0.5 s TWT). These depths diverge from those reported by Hu et al. (2013), especially where the IBPF is reported to extend no deeper than 100 m (Figure 10c).

There are differences between seismic data and borehole information that should be considered when comparing the IBPF depth found here which deviates from that of Hu et al. (2013). In general, well information provides the most accurate in situ measurement but its accuracy is restricted to the location of the well. In the vicinity of the shelf break, the well coverage is very sparse, particularly where our seismic lines are located. There, the $IBPF_F$ depth of Hu et al. (2013) is not tightly constrained and mainly relies on the interpolation of distant wells. Local changes may not be detected in this way.

Furthermore, in seismic data, the vertical positioning of horizons is limited by the vertical seismic resolution. In our data, the vertical resolution is ∼17–23 m (λ/4: 28 Hz, 2,000–2,600 m/s). Consequently, an uncertainty for the depth estimation from seismic data has to be considered.

Finally, seismic data depend on the acoustic properties only, that is, density and seismic velocity. Hu et al. (2013) mention the complexity of identifying IBPF by seismic velocity. Changes in lithology, degree of compaction, porosity, temperature, salinity and fluids in pore space can shift the seismic velocity in permafrost. In consequence, Hu et al. (2013) used different properties for example, temperature, sonic transit time and sonic velocity, resistivity, density, gamma ray and spontaneous potential for identifying the IBPF depths, while resistivity

surveys served as the main indicator of identifying those IBPF depths. However, changes in resistivity at the $IBPF_F$ or $IBPF_P$ were not necessarily accompanied by a defined change in seismic velocity. For instance, the authors mention having found an IBPF zone without a high-velocity interval. However, a defined change in seismic velocity (and/or density) would be necessary to generate a seismic reflection. For slight changes in the velocity, small reflection coefficients at the base of permafrost would generate only low-amplitude reflections that are mostly overprinted by strong free-surface and internal multiples (Duchesne et al., 2022). Therefore, it remains unanswered whether the reflection we detected marks the same boundary of IBPF as inferred by Hu et al. (2013).

7.2.5. The Gas Hydrates Stability Zone

Evidence for the BGHSZ in the Canadian Beaufort Sea was already investigated by Riedel et al. (2017), who pointed out the consistency of the observed BGHSZ with typical characteristics associated with BSRs in deep-water marine environments. These characteristics usually comprise a polarity reversal, a cross-cutting of prevailing structure, an enhanced reflectivity beneath, and high-amplitudes terminated updip at the BGHSZ (Riedel et al., 2017). The BGHSZ reflections we observe fulfill each of these characteristics.

Riedel et al. (2017) provide a map of the extent of gas hydrate occurrences from seismic data in the southern Beaufort Sea. However, the depth of the BGHSZ is not established in detail in the Canadian Beaufort Sea (Pelletier & Medioli, 2014; Riedel et al., 2017), but generally, it is deeper than 1 km in the central shelf (see Figures 1b and 2). To estimate the depth of the BGHSZ reflections, we compare the two-way-travel time with well information in Hu et al. (2015). We infer the maximum depth of the BGHSZ reflections to be ∼1,300 m, ∼1,100 m and ∼980 m on the profiles shown in Figures 7–9, respectively, which is in accordance with the findings of Pelletier and Medioli (2014) and the calculations and observations from Riedel et al. (2017). South of Figure 9, we observe a decrease in depth of the BGHSZ to less than 1,000 m toward an area where the BGHSZ is supposed to be shallower after Pelletier and Medioli (2014) (Figures 1b and 2).

Unlike results from the synthetic seismic data (Figure 5), we did not identify reflections indicating the top of gas hydrates either intra-permafrost or sub-permafrost. Possible reasons are insufficient impedance contrasts for intra-permafrost gas hydrates and sub-permafrost gas hydrate thicknesses that are smaller than the seismic resolution. For example, gas hydrate zones at the Mallik gas hydrate field on Richards Island on the coast of the Beaufort Sea (Figure 1) show thicknesses between 37 and 51 m (Dallimore & Collett, 2005). There, zone B (51 m thick) consists of a "series of 5–10 m thick gas hydrate-bearing sand units separated by 0.5–1 m thick gas hydrate-free silt layers," which possess heterogeneous gas hydrate saturations. A seismic response from such gas hydrate-composed layers may not be explicit, particularly with our seismic resolution of c. 17–23 m ($\lambda/4$: 28 Hz; 2,000–2,600 m/s). However, in addition to these methodological limitations, residual acquisition and processing artifacts may further impede the identification of low-amplitude thin layers.

8. Summary and Conclusions

Multichannel seismic reflection data are suitable for detecting and mapping submarine permafrost and permafrost-associated gas hydrates as specific indicators are included in the seismic response of those features. However, appropriate seismic imaging of the shallow shelf environment in combination with submarine permafrost requires intense seismic processing to attenuate high multiple energy. Synthetic shot gathers of a representative viscoelastic model allow us to minimize the misinterpretation of misleading acquisition and processing artifacts and evaluate the ability of seismic methods to detect submarine permafrost- and gas hydrate-related reflections.

Seismic reflection data collected on the Canadian Beaufort Shelf enable us to make the following observations. First, the top of IBPF has a pronounced high-amplitude reflection that coincides with a loss of acoustic penetration in SBP data. Second, velocity pull-ups and amplitude variations indicate the general presence of IBPF. Third, cross-cutting, negative-polarity and upward-bending reflections indicate the BIBPF as well as the BGHSZ. The latter is accompanied by negative-polarity bright spots and high-amplitude reflectivity beneath indicative of the accumulation of trapped free fluids. However, we do not observe distinct indications for the top of gas hydrates.

Uncertainty remains whether the base of the acoustically detected IBPF describes the outermost physical boundary of IBPF. This uncertainty arises because seismic imaging requires a distinct impedance contrast which may not be fully developed at slushy boundaries, that is, where permafrost conditions change from ice-bonding to partially

ice-bonding. However, we can still define the extent of the submarine permafrost and permafrost-associated gas hydrates. Consequently, this study confirms that the present extent of submarine permafrost reaches the outer continental shelf in the Canadian Beaufort Sea and further supports the concept of submarine permafrost and gas hydrate evolution as described from previous numerical models.

Data Availability Statement

The seismic data used in this study can be found at the Korea Polar Data Center: https://dx.doi.org/doi:10.22663/KOPRI-KPDC-00001958.3 (Kang et al., 2023).

Acknowledgments
This study is funded by the German Research Foundation (DFG Grants KR2222/27-1 and RI2107/3-1) and by the Korean Ministry of Oceans and Fisheries (KIMST, 20210632). This work benefited from the support of the Environmental Geoscience Program of the Geological Survey of Canada (GSC) and is part of an ongoing international collaboration between the GSC, Monterey Bay Aquarium Research Institute, KOPRI and several university partners in Canada and Germany to assess the geohazard potential and environmental impacts of permafrost degradation in the Canadian Beaufort Sea. We further like to acknowledge the crew and scientific staff of the IBRV ARAON during expeditions ARA04C and ARA05C. We would like to thank Schlumberger for providing the VISTA Desktop Seismic Data Processing software (Version 2020), IHS for the Kingdom software (Version 2021) and ESRI for ArcGIS 10.6 under Academic User License Agreements. Figure 8a* was reprinted from Riedel et al. (2017), with permission from Elsevier. Open Access funding enabled and organized by Projekt DEAL.

References

Angelopoulos, M., Overduin, P. P., Miesner, F., Grigoriev, M. N., & Vasiliev, A. (2020). Recent advances in the study of Arctic submarine permafrost. *Permafrost and Periglacial Processes*, *31*(3), 442–453. https://doi.org/10.1002/ppp.2061

Batchelor, C. L., Dowdeswell, J. A., & Pietras, J. T. (2013). Seismic stratigraphy, sedimentary architecture and palaeo-glaciology of the Mackenzie Trough: Evidence for two Quaternary ice advances and limited fan development on the western Canadian Beaufort Sea margin. *Quaternary Science Reviews*, *65*, 73–87. https://doi.org/10.1016/j.quascirev.2013.01.021

Bellefleur, G., Riedel, M., Brent, T., Wright, F., & Dallimore, S. R. (2007). Implication of seismic attenuation for gas hydrate resource characterization, Mallik, Mackenzie Delta, Canada. *Journal of Geophysical Research*, *112*(B10), B10311. https://doi.org/10.1029/2007JB004976

Bellefleur, G., Riedel, M., Huang, J., Saeki, T., Milkereit, B., Ramachandran, K., & Brent, T. A. (2012). Seismic characterization of gas hydrate accumulations in a permafrost environment: Lessons learned from Mallik, Northwest Territories, Canada. In *Scientific results from the JOGMEC/NRCan/Aurora Mallik 2007–2008 Gas Hydrate Production Research Well Program, Mackenzie Delta, Northwest Territories, Canada*. https://doi.org/10.4095/292086

Blasco, S. M., Bennett, R., Brent, T. A., Burton, M., Campbell, P., Carr, E., et al. (2013). 2010 state of knowledge: Beaufort Sea seabed geohazards associated with offshore hydrocarbon development. *Geological Survey of Canada Open File Report*, *6989*, 1–340. https://doi.org/10.4095/292616

Brigham, J. K., & Miller, G. H. (1983). Paleotemperature estimates of the Alaskan Arctic coastal plain during the last 125,000 years. In *Permafrost—4th International Conference* (pp. 80–85). Retrieved from https://www.arlis.org/docs/vol1/ICOP/10368063.pdf

Brothers, L. L., Hart, P. E., & Ruppel, C. D. (2012). Minimum distribution of subsea ice-bearing permafrost on the U.S. Beaufort Sea continental shelf. *Geophysical Research Letters*, *39*(15), L15501. https://doi.org/10.1029/2012GL052222

Brothers, L. L., Herman, B. M., Hart, P. E., & Ruppel, C. D. (2016). Subsea ice-bearing permafrost on the U.S. Beaufort Margin: 1. Minimum seaward extent defined from multichannel seismic reflection data. *Geochemistry, Geophysics, Geosystems*, *17*(11), 4354–4365. https://doi.org/10.1002/2016GC006584

Butler, P. (2012). Strong noise—Removal and replacement on seismic data. *CSEG Recorder*, *37*(9), 34–37.

Carmack, E. C., Macdonald, R. W., & Papadakis, J. E. (1989). Water mass structure and boundaries in the Mackenzie shelf estuary. *Journal of Geophysical Research*, *94*(C12), 18043. https://doi.org/10.1029/JC094iC12p18043

Dallimore, S. R., & Collett, T. S. (1998). Gas hydrates associated with deep permafrost in the Mackenzie delta, NWT, Canada: Regional overview. In *Proceedings of the 7th International Conference on Permafrost* (Vol. 55, pp. 201–206). Retrieved from https://www.arlis.org/docs/vol1/ICOP/40770716/CD-ROM/Proceedings/PDF001189/032141.pdf

Dallimore, S. R., & Collett, T. S. (2005). Summary and implications of the Mallik 2002 gas hydrate production research well program. In *Geological Survey of Canada, Bulletin* (Vol. 585). https://doi.org/10.4095/220714

Dallimore, S. R., Paull, C. K., Taylor, A. E., Riedel, M., MacAulay, H. A., Côté, M. M., & Jin, Y. K. (2015). Geohazard investigations of permafrost and gas hydrates in the outer shelf and upper slope of the Canadian Beaufort Sea. In *Proceedings of a Symposium to Commemorate the Contributions of J. Ross Mackay (1915–2014) to Permafrost Science in Canada, 7th Canadian Permafrost Conference* (pp. 37–42).

Dallimore, S. R., Uchida, T., & Collett, T. S. (1999). Scientific results from JAPEX/JNOC/GSC Mallik 2L-38 gas hydrate research well, Mackenzie Delta, Northwest Territories, Canada. https://doi.org/10.4095/210723

Dewing, K., Brake, V., Duchesne, M. J., Brent, T. A., & Joyce, N. (2016). Stratigraphy and structure of the Drake Point Anticline, Sabine Peninsula, Canadian Arctic Islands. *Canadian Journal of Earth Sciences*, *53*(12), 1484–1500. https://doi.org/10.1139/cjes-2016-0030

Dietrich, J. R., Chen, Z., Chi, G., Dixon, J., & Hu, K. (2011). Petroleum plays in upper Cenozoic strata in the Beaufort-Mackenzie Basin, Arctic Canada. *Search and Discovery*, *10300*. https://doi.org/10.1029/2006GL027977.4

Dixon, J. (1996). In J. Dixon (Ed.), *Geological atlas of the Beaufort-Mackenzie area*. Natural Resources Canada. https://doi.org/10.4095/207658

Dixon, J., & Dietrich, J. R. (1990). Canadian Beaufort Sea and adjacent land areas. In A. Grantz, L. Johnson, & J. F. Sweeney (Eds.), *The Arctic Ocean Region* (Vol. 50, pp. 239–256). Geological Society of America. https://doi.org/10.1130/dnag-gna-l.239

Dixon, J., Dietrich, J. R., & McNeil, D. H. (1992). Upper Cretaceous to Pleistocene sequence stratigraphy of the Beaufort-Mackenzie and Banks Island areas, northwest Canada. In *Geological Survey of Canada, Bulletin* (Issue 407). https://doi.org/10.4095/133237

Dixon, J., Lane, L. S., Dietrich, J. R., McNeil, D. H., & Chen, Z. (2019). Geological history of the Late Cretaceous to Cenozoic Beaufort-Mackenzie Basin, Arctic Canada. In A. D. Miall (Ed.), *The Sedimentary Basins of the United States and Canada* (2nd ed., pp. 695–717). Elsevier. https://doi.org/10.1016/B978-0-444-63895-3.00017-6

Dobinski, W. (2011). Permafrost. *Earth-Science Reviews*, *108*(3–4), 158–169. https://doi.org/10.1016/j.earscirev.2011.06.007

Dondurur, D. (2018). Chapter 12—Specific methods. In D. Dondurur (Ed.), *Acquisition and processing of marine seismic data* (pp. 549–584). Elsevier. https://doi.org/10.1016/B978-0-12-811490-2.00012-8

Draebing, D. (2016). Application of refraction seismics in alpine permafrost studies: A review. *Earth-Science Reviews*, *155*, 136–152. https://doi.org/10.1016/j.earscirev.2016.02.006

Duchesne, M. J., Fabien-Ouellet, G., & Bustamante, J. (2022). Detecting subsea permafrost layers on marine seismic data: An appraisal from forward modelling. *Near Surface Geophysics*, *21*(1), 3–20. https://doi.org/10.1002/nsg.12231

Dyke, A. S. (2004). An outline of North American deglaciation with emphasis on central and northern Canada. In J. Ehlers, P. L. Gibbard, & P. D. Hughes (Eds.), *Quaternary Glaciations - Extent and Chronology* (Vol. 2, pp. 373–424). Elsevier. https://doi.org/10.1016/S1571-0866(04)80209-4

Fabien-Ouellet, G., Duchesne, M. J., & Bustamante Restrepo, J. (2020). Seismic characterization of subsea permafrost: Insights from viscoelastic modeling. *SEG Technical Program Expanded Abstracts*, 1024–1028. https://doi.org/10.1190/segam2020-3399580.1

Fabien-Ouellet, G., Gloaguen, E., & Giroux, B. (2017). Time domain viscoelastic full waveform inversion. *Geophysical Journal International*, *209*(3), 1718–1734. https://doi.org/10.1093/gji/ggx110

Frederick, J. M., & Buffett, B. A. (2015). Effects of submarine groundwater discharge on the present-day extent of relict submarine permafrost and gas hydrate stability on the Beaufort Sea continental shelf. *Journal of Geophysical Research: Earth Surface*, *120*(3), 417–432. https://doi.org/10.1002/2014JF003349

Gwiazda, R., Paull, C. K., Dallimore, S. R., Melling, H., Jin, Y. K., Hong, J. K., et al. (2018). Freshwater Seepage into sediments of the shelf, shelf edge, and continental slope of the Canadian Beaufort Sea. *Geochemistry, Geophysics, Geosystems*, *19*(9), 3039–3055. https://doi.org/10.1029/2018GC007623

Harris, S. A., French, H. M., Heginbottom, J. A., Johnston, G. H., Ladanyi, B., Sego, D. C., & van Everdingen, R. O. (1988). Glossary of permafrost and related ground-ice terms. In *Arctic and alpine research* (Vol. 21, Issue 2). https://doi.org/10.2307/1551636

Hinz, K., Delisle, G., & Block, M. (1998). Seismic evidence for the depth extent of permafrost in shelf sediments of the Laptev Sea, Russian Arctic? In *PERMAFROST - 7th International Conference* (Vol. 55, pp. 453–457). Retrieved from https://www.arlis.org/docs/vol1/ICOP/40770716/CD-ROM/Proceedings/PDF001189/070244.pdf

Hu, K., Brent, T. A., Issler, D. R., & Chen, Z. (2015). Synthetic seismograms from borehole seismic data and well logs, Beaufort-Mackenzie Basin. https://doi.org/10.4095/296213

Hu, K., Dietrich, J. R., Chen, Z., & Hannigan, P. K. (2018). Petrophysical analyses of hydrocarbon reservoirs and overpressure zones in Tertiary deep-marine strata in the northern Beaufort-Mackenzie Basin, Arctic Canada. In *Geological Survey of Canada Open File 8368*. https://doi.org/10.4095/306960

Hu, K., Issler, D. R., Chen, Z., & Brent, T. A. (2013). Permafrost investigation by well logs, and seismic velocity and repeated shallow temperature surveys, Beaufort-Mackenzie Basin. In *Geological Survey of Canada Open File Report* (Issue 6956). https://doi.org/10.4095/293120

IPCC. (2013). In T. F. Stocker, D. Qin, G.-K. Plattner, M. Tignor, S. K. Allen, J. Boschung, et al. (Eds.), *Climate Change 2013: The Physical Science Basis. Contribution of Working Group I to the Fifth Assessment Report of the Intergovernmental Panel on Climate Change*. Cambridge University Press. Retrieved from https://www.ipcc.ch/report/ar5/wg1/

Jakobsson, M., Mayer, L. A., Bringensparr, C., Castro, C. F., Mohammad, R., Johnson, P., et al. (2020). The International Bathymetric Chart of the Arctic Ocean Version 4.0. *Scientific Data*, *7*(1), 1–14. https://doi.org/10.1038/s41597-020-0520-9

Jin, Y. K., & Dallimore, S. R. (2016). ARA05C Marine Research Expedition Canada-Korea-USA Beaufort Sea Geoscience Research Program: Summary of 2014 activities. *Geological Survey of Canada, Open File, 7999*. https://doi.org/10.4095/297866

Jin, Y. K., Riedel, M., Hong, J. K., Nam, S. I., Jung, J. Y., Ha, S. Y., et al. (2015). Overview of field operations during a 2013 research expedition to the southern Beaufort Sea on the RV Araon. *Geological Survey of Canada, Open File, 7754*. https://doi.org/10.4095/295856

Johansen, T. A., Digranes, P., van Schaack, M., & Lønne, I. (2003). Seismic mapping and modeling of near-surface sediments in polar areas. *Geophysics*, *68*(2), 566–573. https://doi.org/10.1190/1.1567226

Kang, S.-G., Jin, Y. K., & Hong, J. K. (2023). Geophysical data (MCS and SBP) collected during the 2013 ARA04C and 2014 ARA05C expeditions on the Beufort Sea [Dataset]. Korea Polar Data Center. https://doi.org/10.22663/KOPRI-KPDC-00001958.3

Kang, S.-G., Jin, Y. K., Jang, U., Duchesne, M. J., Shin, C., Kim, S., et al. (2021). Imaging the P-wave velocity structure of Arctic subsea permafrost using Laplace-domain full-waveform inversion. *Journal of Geophysical Research: Earth Surface*, *126*(3), 1–15. https://doi.org/10.1029/2020JF005941

King, M. S., Zimmerman, R. W., & Corwin, R. F. (1988). Seismic and electrical properties of unconsolidated permafrost. *Geophysical Prospecting*, *36*(4), 349–364. https://doi.org/10.1111/j.1365-2478.1988.tb02168.x

Kvenvolden, K. A. (1993). Gas hydrates-geological perspective and global change. *Reviews of Geophysics*, *31*(2), 173–187. https://doi.org/10.1029/93RG00268

Lane, L. S., & Dietrich, J. R. (1995). Tertiary structural evolution of the Beaufort Sea-Mackenzie Delta region, Arctic Canada. *Bulletin of Canadian Petroleum Geology*, *43*(3), 293–314. https://doi.org/10.35767/gscpgbull.43.3.293

Lewis, K. A., & Collett, T. S. (2013). Brookian sequence well log correlation sections and occurrence of gas hydrates, North-Central North Slope, Alaska. *U.S. Geological Survey Scientific Investigations Report 2013-5050, 23*. Retrieved from http://pubs.er.usgs.gov/publication/sir20135050

Liu, J., Zhang, J., Ma, F., Wang, M., & Sun, Y. (2017). Estimation of seismic velocities and gas hydrate concentrations: A case study from the Shenhu area, northern South China Sea. *Marine and Petroleum Geology*, *88*, 225–234. https://doi.org/10.1016/j.marpetgeo.2017.08.014

MacAulay, H. A., & Hunter, J. A. (1982). Detailed seismic refraction analysis of ice-bonded permafrost layering in the Canadian Beaufort Sea. In *Proceedings of the 4th Canadian Permafrost Conference* (pp. 256–267).

Majorowicz, J. A., & Hannigan, P. K. (2000). Stability zone of natural gas hydrates in a permafrost-bearing region of the Beaufort-Mackenzie Basin: Study of a feasible energy source (geological survey of Canada Contribution No. 1999275). In *Natural Resources Research* (Vol. 9, Issue 1). https://doi.org/10.1023/A:1010105628952

Majorowicz, J. A., & Osadetz, K. G. (2001). Gas hydrate distribution and volume in Canada. *AAPG Bulletin*, *85*(7), 1211–1230. https://doi.org/10.1306/8626CA9B-173B-11D7-8645000102C1865D

Matson, R., Wolf, K., & Yancey, D. (2013). Influence of permafrost on seismic imaging in Alaska. In *Society of Petroleum Engineers - SPE Arctic and Extreme Environments Conference and Exhibition, AEE 2013* (Vol. 1, pp. 76–102). https://doi.org/10.2118/166821-ms

McLaughlin, F., Carmack, E., Macdonald, R., Melling, H., Swift, J., Wheeler, P., et al. (2004). The joint roles of Pacific and Atlantic-origin waters in the Canada Basin, 1997–1998. *Deep Sea Research Part I: Oceanographic Research Papers*, *51*(1), 107–128. https://doi.org/10.1016/j.dsr.2003.09.010

Natali, S. M., Holdren, J. P., Rogers, B. M., Treharne, R., Duffy, P. B., Pomerance, R., & MacDonald, E. (2021). Permafrost carbon feedbacks threaten global climate goals. *Proceedings of the National Academy of Sciences*, *118*(21), e2100163118. https://doi.org/10.1073/pnas.2100163118

Osterkamp, T. E. (2001). Sub-sea permafrost. In *Encyclopedia of Ocean Sciences* (Vol. 2, pp. 2902–2912). Elsevier. https://doi.org/10.1006/rwos.2001.0008

Patruno, S., Hampson, G. J., & Jackson, C. A. L. (2015). Quantitative characterisation of deltaic and subaqueous clinoforms. *Earth-Science Reviews*, *142*, 79–119. https://doi.org/10.1016/j.earscirev.2015.01.004

Paull, C. K., Dallimore, S. R., Caress, D. W., Gwiazda, R., Melling, H., Riedel, M., et al. (2015). Active mud volcanoes on the continental slope of the Canadian Beaufort Sea. *Geochemistry, Geophysics, Geosystems*, *16*(9), 3160–3181. https://doi.org/10.1002/2015GC005928.Received

Paull, C. K., Dallimore, S. R., Hughes-Clarke, J., Blasco, S. M., Lundsten, E., Ussler, W., et al. (2011). Tracking the decomposition of submarine permafrost and gas hydrate under the shelf and slope of the Beaufort Sea.

Paull, C. K., Dallimore, S. R., Jin, Y. K., Caress, D. W., Lundsten, E., Gwiazda, R., et al. (2022). Rapid seafloor changes associated with the degradation of Arctic submarine permafrost. *Proceedings of the National Academy of Sciences*, *119*(12), e2119105119. https://doi.org/10.1073/pnas.2119105119

Paull, C. K., Ussler, W., Dallimore, S. R., Blasco, S. M., Lorenson, T. D., Melling, H., et al. (2007). Origin of pingo-like features on the Beaufort Sea shelf and their possible relationship to decomposing methane gas hydrates. *Geophysical Research Letters*, *34*(1), L01603. https://doi.org/10.1029/2006GL027977

Pelletier, B. R., & Medioli, B. E. (2014). Environmental atlas of the Beaufort coastlands. In *Geological Survey of Canada, Open File* (Vol. 7619). https://doi.org/10.4095/294601

Portnov, A., Smith, A. J., Mienert, J., Cherkashov, G., Rekant, P., Semenov, P., et al. (2013). Offshore permafrost decay and massive seabed methane escape in water depths >20 m at the South Kara Sea shelf. *Geophysical Research Letters*, *40*(15), 3962–3967. https://doi.org/10.1002/grl.50735

Pullan, S., MacAulay, H. A., Hunter, J. A. M., Good, R. L., Gagne, R. M., & Burns, R. A. (1987). Permafrost distribution determined from seismic refraction. In B. R. Pelletier (Ed.), *Marine Science Atlas of the Beaufort Sea: Geology and Geophysics*. https://doi.org/10.4095/126967

Ramachandran, K., Bellefleur, G., Brent, T., Riedel, M., & Dallimore, S. R. (2011). Imaging permafrost velocity structure using high resolution 3D seismic tomography. *Geophysics*, *76*(5), B187–B198. https://doi.org/10.1190/geo2010-0353.1

Rekant, P., Bauch, H. A., Schwenk, T., Portnov, A., Gusev, E., Spiess, V., et al. (2015). Evolution of subsea permafrost landscapes in Arctic Siberia since the Late Pleistocene: A synoptic insight from acoustic data of the Laptev Sea. *Arktos*, *1*(1), 11. https://doi.org/10.1007/s41063-015-0011-y

Rekant, P., Cherkashev, G., Vanstein, B., & Krinitsky, P. (2005). Submarine permafrost in the nearshore zone of the southwestern Kara Sea. *Geo-Marine Letters*, *25*(2–3), 183–189. https://doi.org/10.1007/s00367-004-0199-5

Rekant, P., & Vasiliev, A. (2011). Periglacial processes on arctic shelf and coast: Offshore permafrost in the Kara Sea. *Earth's Cryosphere*, *15*(4), 60–62.

Riedel, M., Bellefleur, G., Dallimore, S. R., Taylor, A., & Wright, J. F. (2006). Amplitude and frequency anomalies in regional 3D seismic data surrounding the Mallik 5L-38 research site, Mackenzie Delta, Northwest Territories, Canada. *Geophysics*, *71*(6), B183–B191. https://doi.org/10.1190/1.2338332

Riedel, M., Bellefleur, G., Mair, S., Brent, T. A., & Dallimore, S. R. (2009). Acoustic impedance inversion and seismic reflection continuity analysis for delineating gas hydrate resources near the Mallik research sites, Mackenzie Delta, Northwest Territories, Canada. *Geophysics*, *74*(5), B125–B137. https://doi.org/10.1190/1.3159612

Riedel, M., Brent, T. A., Taylor, G., Taylor, A. E., Hong, J.-K., Jin, Y.-K., & Dallimore, S. R. (2017). Evidence for gas hydrate occurrences in the Canadian Arctic Beaufort Sea within permafrost-associated shelf and deep-water marine environments. *Marine and Petroleum Geology*, *81*, 66–78. https://doi.org/10.1016/j.marpetgeo.2016.12.027

Riedel, M., Hong, J. K., Jin, Y. K., & Kim, H. S. (2014). Refraction seismic velocity analyses from multichannel seismic data acquired during Expedition ARA04C on the IBRV Araon in the Beaufort Sea. *Geological Survey of Canada, Open File, 7618*. https://doi.org/10.4095/295549

Riedel, M., Hong, J. K., Jin, Y. K., Rohr, K. M. M., & Côté, M. M. (2016). First results on velocity analyses of multichannel seismic data acquired with the icebreaker RV Araon across the southern Beaufort Sea, offshore Yukon. *Geological Survey of Canada, Current Research*, *3*, 24. https://doi.org/10.4095/298840

Ruppel, C. D. (2015). Permafrost-associated gas hydrate: Is it really approximately 1% of the global system? *Journal of Chemical & Engineering Data*, *60*(2), 429–436. https://doi.org/10.1021/je500770m

Ruppel, C. D., & Kessler, J. D. (2017). The interaction of climate change and methane hydrates. *Reviews of Geophysics*, *55*(1), 126–168. https://doi.org/10.1002/2016RG000534

Schuur, E. A. G., McGuire, A. D., Schädel, C., Grosse, G., Harden, J. W., Hayes, D. J., et al. (2015). Climate change and the permafrost carbon feedback. *Nature*, *520*(7546), 171–179. https://doi.org/10.1038/nature14338

Sheriff, R., & Geldart, L. (1995). Characteristics of seismic events. In *Exploration Seismology* (pp. 145–190). Cambridge University Press. https://doi.org/10.1017/CBO9781139168359.007

Shipley, T. H., Houston, M. H., Buffler, R. T., Shaub, F. J., McMillen, K. J., Laod, J. W., & Worzel, J. L. (1979). Seismic evidence for widespread possible gas hydrate horizons on continental slopes and rises. *AAPG Bulletin*, *63*(12), 2204–2213. https://doi.org/10.1306/2F91890A-16CE-11D7-8645000102C1865D

Smith, S. L., & Judge, A. S. (1993). Gas hydrate database for Canadian Arctic and selected east coast wells. https://doi.org/10.4095/192438

Spence, G. D., Haacke, R. R., & Hyndman, R. D. (2010). 4. Seismic indicators of natural gas hydrate and underlying free gas. In *Geophysical characterization of gas hydrates* (pp. 39–71). Society of Exploration Geophysicists. https://doi.org/10.1190/1.9781560802197.ch4

Taylor, A. E., Dallimore, S. R., Hill, P. R., Issler, D. R., Blasco, S. M., & Wright, F. (2013). Numerical model of the geothermal regime on the Beaufort Shelf, Arctic Canada since the Last interglacial. *Journal of Geophysical Research: Earth Surface*, *118*(4), 2365–2379. https://doi.org/10.1002/2013JF002859

Taylor, A. E., Dallimore, S. R., & Outcalt, S. I. (1996). Late Quaternary history of the Mackenzie–Beaufort region, Arctic Canada, from modelling of permafrost temperatures. 1. The onshore–offshore transition. *Canadian Journal of Earth Sciences*, *33*(1), 52–61. https://doi.org/10.1139/e96-006

van Everdingen, R. O. (1998). *Multi-language glossary of permafrost and related ground-ice terms* (revised ed. 2005, p. 159). International Permafrost Association. Retrieved from https://globalcryospherewatch.org/reference/glossary_docs/Glossary_of_Permafrost_and_Ground-Ice_IPA_2005.pdf

Verschuur, D. J. (2013). *Seismic multiple removal techniques: Past, present and future* (revised ed.). EAGE Publications.

Weaver, J. S., & Stewart, J. M. (1982). In situ hydrates under the Beaufort Sea shelf. In *Proceedings of the 4th Canadian Permafrost Conference* (pp. 312–319).

Westbrook, G. K., Chand, S., Rossi, G., Long, C., Bünz, S., Camerlenghi, A., et al. (2008). Estimation of gas hydrate concentration from multi-component seismic data at sites on the continental margins of NW Svalbard and the Storegga region of Norway. *Marine and Petroleum Geology*, *25*(8), 744–758. https://doi.org/10.1016/J.MARPETGEO.2008.02.003

Wood, W. T., Stoffa, P. L., & Shipley, T. H. (1994). Quantitative detection of methane hydrate through high-resolution seismic velocity analysis. *Journal of Geophysical Research*, *99*(B5), 9681–9695. https://doi.org/10.1029/94JB00238

Yun, T. S., Francisca, F. M., Santamarina, J. C., & Ruppel, C. D. (2005). Compressional and shear wave velocities in uncemented sediment containing gas hydrate. *Geophysical Research Letters*, *32*(10), L10609. https://doi.org/10.1029/2005GL022607

Zhang, G., Hao, C., & Yao, C. (2018). Analytical study of the reflection and transmission coefficient of the submarine interface. *Acta Geophysica*, *66*(4), 449–460. https://doi.org/10.1007/s11600-018-0153-y